Title

Advancing Linear and Nonlinear Optical Microscopy with Optical Sectioning Capability for Imaging Live Biological Systems

Author

Pan, Daisong

Publication Date

2024

Peer reviewed|Thesis/dissertation

Advancing Linear and Nonlinear Optical Microscopy with Optical Sectioning Capability for Imaging Live Biological Systems

By
Daisong Pan

A dissertation submitted in partial satisfaction of the
requirements for the degree of
Doctor of Philosophy
in
Physics
in the
Graduate Division
of the
University of California, Berkeley

Committee in charge:

Professor Na Ji, Chair
Professor Laura Waller
Professor Roger Falcone

Fall 2024

Abstract

Advancing Linear and Nonlinear Optical Microscopy with Optical Sectioning Capability for Imaging Live Biological Systems

by

Daisong Pan

Doctor of Philosophy in Physics

University of California, Berkeley

Professor Na Ji, Chair

A microscope with optical sectioning capability allows for the acquisition of a clear image from a thin slice within a thick sample. In contrast, optical microscopy without such capability has out-of-focus light blurring in-focus details when imaging thick samples, degrading contrast and resolution. For this reason, microscopy modalities with optical sectioning are essential tools for tissue imaging, enabling the acquisition of structural and functional information at high resolution and precision. Various approaches to achieving optical sectioning have been developed, each suited to different application scenarios. This thesis aims to advance the capability and explore the application of three optical microscopy modalities: confocal fluorescence microscopy, three-photon fluorescence (3PF) microscopy and third-harmonic generation (THG) microscopy, categorized into linear and nonlinear imaging, respectively, with a focus on their use in live biological systems. Chapter 1 briefly introduces the imaging modalities involved, the challenges faced by each technology, and the approaches we are employing to address these challenges.

In Chapter 2, this thesis incorporates a novel adaptive optics (AO) approach based on frequency-multiplexed aberration measurement into single-photon confocal fluorescence microscopy. Confocal microscopy achieves optical sectioning by using a confocal pinhole to reject out-of-focus fluorescence light. However, it can be affected by optical aberrations induced by imperfect optics and complex samples, which degrade imaging quality. By correcting optical aberrations affecting both the excitation and emission light with our AO approach, we demonstrate that this method can measure aberrations using signals from features of any size and substantially improve the image quality in both nonbiological and biological samples.

In Chapter 3, this thesis explores the application of combined 3PF and THG microscopy for plant root imaging and shows how AO THG microscopy improves image quality in various living systems. Both 3PF and THG imaging modalities achieve optical sectioning by employing a nonlinear process that generates a signal confined to the focal plane. While the 3PF signal originates from fluorophores, the THG signal arises from inherent local optical heterogeneities, eliminating the need for fluorescent labeling. Combined with the deep penetration capability enabled by near-infrared excitation, we demonstrate *in situ* imaging of live roots and microbes at high spatiotemporal resolution, revealing key plant root structures from the surface to deep within the root. Furthermore, we apply the aforementioned AO approach to THG microscopy, achieving high-resolution *in vivo* imaging within various biological systems.

In Chapter 4, this thesis describes ongoing efforts to develop a homodyne THG microscopy system. To address the challenge of low optical conversion efficiency in THG imaging of biological samples, a homodyne process that employs the coherent mixing of the sample-generated THG signal with a reference THG signal is used to enhance the conversion efficiency. Our home-built THG homodyne microscopy aims to enable long-term imaging of living systems with minimal photodamage, with a specific focus on studies of delicate root structures.

Together, this thesis presents several advancements in optical microscopy techniques and aspires to enable future studies using these improved tools in various live biological systems.

To my beloved grandparents, whose boundless love and unwavering support shaped my life before I embarked on my PhD journey far from home. Even though you left us while I was away, your enduring memory and influence remain with me always.

Contents

Dedication i
Contents ii
List of figures v
List of tables viii
Acknowledgments ix
1. Introduction 1
1.1 Optical sectioning microscopy 1
1.2 Optical aberrations and adaptive optics for confocal microscopy 2
1.3 Three-photon fluorescence (3PF) microscopy and third-harmonic generation (THG) microscopy 3
1.4 Homodyne THG microscopy 4
2. Frequency-Multiplexed Aberration Measurement for Confocal Microscopy 6
2.1 Introduction 6
2.2 Methods 7
2.2.1 AO confocal fluorescence microscope 7
2.2.2 Frequency-multiplexed aberration measurement and correction 7
2.2.3 Practical considerations 8
2.2.4 Bead and fluorescent solution samples 9
2.2.5 Zebrafish preparation and imaging 9
2.2.6 Mouse preparation and imaging 10
2.2.7 Animal experiments 11
2.3 Results 11
2.3.1 System aberration correction of the confocal fluorescence microscope 11
2.3.2 Correction of large aberrations induced by a capillary tube 11
2.3.3 Adaptive optical correction of artificial aberrations using different feature sizes 11
2.3.4 AO correction of biological sample-induced aberrations in vivo 13

2.4 Discussions and conclusions 15
3. Advances in Three-Photon and Third-Harmonic Generation Microscopy for Label-Free Root Imaging 16
3.1 Introduction 16
3.1.1 Introduction to multiphoton fluorescence and harmonic generation microscopy 16
3.1.2 Root biology and plant root imaging 18
3.1.3 Adaptive optics for THG microscopy 19
3.2 Methods and materials 19
3.2.1 3PF and THG imaging of plant roots 19
3.2.2 Adaptive optical THG microscopy 21
3.3 Label-Free Structural Imaging of Plant Roots and Microbes Using THG Microscopy. 23
3.3.1 THG microscopy provides label-free contrast for plant root structures at subcellular resolution 23
3.3.2 THG and 3P autofluorescence microscopy imaging of the mature zone of B. distachyon roots 24
3.3.3 THG and 3P autofluorescence microscopy image meristem and root tip of B. distachyon roots at subcellular resolution 26
3.3.4 THG and 3PF microscopy enable simultaneous imaging of plant roots and microbes in the rhizosphere 29
3.4 Adaptive Optical Third-Harmonic Generation Microscopy for In Vivo Imaging of Tissues 30
3.4.1 AO THG microscope characterization and performance evaluation 30
3.4.2 In vivo plant root imaging 31
3.5 Conclusion and discussion 32
3.5.1 THG microscopy provides great potential for root biology 32
3.5.2 Adaptive Optical THG Microscopy Extends the Application of both AO and THG 34
4. Third-Harmonic Generation Microscopy with Homodyne Detection 35
4.1 Introduction 35
4.2 Optical homodyne detection 36
4.3 Acquiring homodyne-enhanced images with harmonic generation microscopy 37
4.4 System setup 38
4.5 Practical considerations 39

4.6 Current stage and future plans for the project 40
5. Conclusion 41
References 43

List of figures

Fig. 1.1 3PF and THG imaging of non-living samples. (a,b) 3PF and THG images of a periodic micro-additively manufactured lattice structure, fabricated using multiphoton lithography. While THG enables imaging of non-fluorescent structures, the lattice was made from fluorescent materials to allow for side-by-side comparison between the two imaging modalities. Cracks were intentionally introduced, visible in the 3PF signal in (a), to demonstrate THG's capability in non-destructive defect examination. As shown in (b), THG provides enhanced contrast at the defect sites due to abrupt changes in refractive index. (c,d) THG imaging of chemical reactions in heterogeneous media via phase transformation, with enhanced contrast at the phase separation boundaries within droplets due to differing optical properties. (d) A zoomed-in view of the yellow box in (c), showing the site of phase separation rotating over 9 consecutive time points. 4

Fig. 2.1 AO confocal fluorescent microscopy. (a) Schematics of microscope. (b) Frequency-multiplexed aberration measurement. Left: DM divided into modulated (yellow) and fixed (grey) segments. Middle: FT magnitude (magenta) and phase (orange) of example signal trace from tilt and phase measurement, respectively. Right: 2D FT magnitude vs. tip/tilt maps of all DM segments. (c) XY and YZ PSFs measured with a 0.2-μm-diameter bead before and after system AO correction. (d) Corrective wavefront for system aberration. (e) Lateral and axial signal profiles along yellow lines in (c). (c)-(e) 0.6 AU pinhole. (f) 1-μm-diameter fluorescent beads in a capillary tube. (g) XY, XZ, YZ images of a 1-μm-diameter bead before AO correction. (h) Corrective wavefront. (i) XY, XZ, YZ images after AO correction. (j) Maximum intensity projection (MIP) of a 25-μm-thick image stack over 250-μm × 150-μm field of view before and after AO, respectively. (f)-(j) 1.2 AU pinhole. 22.6× and 20.3× digital gains for No AO images in (g,j), respectively, to increase visibility. Scale bars: Right panel in (b) 10 μm, (c) 0.5 μm, (i) 2 μm, (j) 10 μm. Post-objective power for aberration measurement: (c)-(e) 0.9 μW, (f)-(j) 0.3-3.9 μW; for image acquisition: (c) 3.2 μW, (g)-(j) 1.9 μW..... 10

Fig. 2.2 Performance of frequency-multiplexed measurements of artificial aberrations using signal of 0.2-μm-diameter beads, 4-μm-diameter beads, or fluorescent solution, respectively. (a)-(d) Axial FWHM (normalized to aberration-free axial FWHM, blue curves, left axis) for two bead samples and signal (normalized to aberration-free signal, red curves, right axis) versus AO iteration number. Insets: applied artificial aberrations. (a) Astigmatism; (b) Coma; (c) Spherical aberration (SA); (d) Trefoil. 0.6 AU pinhole size. Post-objective power for aberration measurement: 0.2 μW-0.7 mW. 12

Fig. 2.3 AO improves confocal imaging quality by correcting biological-sample-induced aberrations. (a) MIPs of a 6.25-μm-thick image stack taken without and with AO when imaging 0.2-μm-diameter fluorescent beads through a zebrafish larva. Insets: spatial frequency space representations; dashed circles: (0.5 μm)-1. AO was performed on the bead in the orange box. (b) FT magnitude vs. tip/tilt displacement maps from 1st iteration of AO.

(c) Corrective wavefront for (a). (d) XY and XZ images of the bead in the orange boxes in (a) without and with AO. (e) Peak signal of the bead in (d) over iterations. (f) XY images of Alexa 647-labeled somite outlines of a zebrafish larva without and with AO. Insets: YZ images along the red dashed line. (g) FT magnitude vs. tip/tilt displacement maps from 4th iteration of AO. (h) Corrective wavefront for (f). (i) Signal profiles along the dashed lines 1 and 2 in (f). (j) XY images of miRFP680-labeled neurons and XZ images along the white line acquired without and with AO. (k) Corrective wavefront for (j). (l) Signal profiles along the dashed lines 3 and 4 in (j). (a-e, j-l) 0.6 AU pinhole. (f- i) 1.2AU pinhole. 6.1× and 5.1× digital gains for No AO images in (a) and (d), respectively, to increase visibility. Red boxes in (b, g): segments without measurable interference magnitudes. Scale bar: (a) 5 μm, (b) 10 μm, (d) 1 μm, (f) XY images, 10 μm; insets, 2 μm, (g) 10 μm, (j) XY images, 20 μm; XZ images, 5 μm. Post-objective power for aberration measurement: (a- e) 0.5-2.1 μW, (f- i) 2.7-3.3 μW, (j- l) 16-17 μW; for image acquisition: (a, d) 1.2 μW, (f) 3.3 μW, (j) 16 μW. 14

Fig. 3.1 THG microscopy reveals plant root structure at subcellular resolution. (a) Schematics of the microscope and EcoFAB. Red: excitation light; Green: 3P fluorescence; blue: THG. X, Y: X and Y galvanometer mirrors; M: mirror; Dm: dichroic mirror; PMT: photomultiplier tube. Insets: lateral (xy) and axial (xz, yz) images of a 0.2-μm-diameter bead. (b) xz THG image of the interface between coverglass and growth medium. (c) xz and (d,e) xy THG images of *B. distachyon* roots inside the EcoFAB chamber. (b,c) acquired at 2 μm/pixel in X and 1 μm/pixel in Z. (d,e) acquired at 1 μm/pixel. (f) Brightest-spot projection with depth cueing (100% to 50%) of an 88-μm-thick image stack of a root tip acquired at 0.8 μm/pixel and z step size of 2.75 μm. White arrows: border-like cells. Post-objective power: (b) 2 mW, (c,d) 3 mW, (e) 4 mW, (f) 2.4-2.8 mW. 23

Fig. 3.2 3P autofluorescence and THG microscopy visualize epidermis, cortex, endodermis, and vasculature in the mature root zone of *B. distachyon* roots. (a) 3P autofluorescence (green) and THG (cyan) xz images acquired at 1 μm/pixel showing a cross section of mature root zone. (b-d) xy images acquired at depths indicated by white arrows in a corresponding to putative (b) epidermis, (c) cortex and (d) endodermis tissues. Pixel size: 1 μm/pixel. (e) xy THG images of root tissues at 26 μm, 80 μm, and 140 μm depths, corresponding to putative epidermis, endodermis and vasculature, respectively. Pixel size: 0.3 μm/pixel. Post-objective powers: (a-d) 2.6 mW, (e) 1.2, 1.6, and 14 mW from left to right. 25

Fig. 3.3 3P autofluorescence and THG microscopy provide label-free imaging of the *B. distachyon* root meristem at subcellular resolution. (a) 3P autofluorescence (green) and THG (cyan) xz images acquired at 0.3 μm/pixel showing a cross section of the root meristem. White arrow: putative Casparian strip. (b-e) 3P autofluorescence (green) and THG (cyan) xy images acquired at (b,c) 0.5 μm/pixel and (d,e) 0.3 μm/pixel. Yellow arrows: putative nucleoli; Dashed white box: a mitotic cell; red arrow: nascent cell wall. Post-objective power: (a) 5.3 mW; (b,c) 5 mW; (d,e) 7 mW. 27

Fig. 3.4 THG imaging of *B. distachyon* apical meristem and root cap. (a) Brightest-spot projection with depth cueing (100% to 50%) of an image stack through a root tip. 230-μm-thick image stack acquired at 1 μm/pixel and z step size of 2 μm. (b) xy image acquired at z=160 μm. White arrows in a,b: boundary between meristem and root cap. (c) xz images acquired along dashed yellow line in a. (d,e) xy images from two other root samples acquired at 0.5 μm/pixel. These roots were placed in between a microscope slide and a coverslip instead of inside

EcoFAB to minimize sample motion. Post-objective power: (a-c) 3-15 mW; (d) 4mW; (e) 3.4 mW. 28

Fig. 3.5 Imaging root-microbe interactions at high spatial and temporal resolution. (a) 3PF (green) and THG (cyan) xy images of *A. thaliana* root inoculated with two strains of *P. simiae* (wildtype *P. simiae* labeled with GFP, mutant *P. simiae* without GFP). (b) Consecutive frames of time-lapse imaging of the dashed box area in a with 3PF in green and THG in gray. Red/purple, yellow, and orange arrowheads: stationary, slowly-moving, fast-moving bacteria, respectively. (c,d) Maximal intensity projected 3PF (yellow) and THG (cyan) images of *B. distachyon* roots inoculated with *T. atroviride* strain IMI with GFP-labeled nuclei. (c) 50-μm-thick image stack acquired at 0.75 μm/pixel and z step size of 2.5 μm. (d) 70-μm-thick image stacks acquired at 0.5 μm/pixel and z step size of 2.5 μm. White arrowheads: GFP-labeled nuclei; pink arrowheads: unlabeled nuclei; white arrows: spores. Insets: zoomed-in views of white dashed boxes. Post-objective power: (a, b) 3.4 mW; (c) 5.6mW; (d) 5.3 mW. 29

Fig. 3.6 Schematics of the AO THG microscope and system aberration correction, AO improves THG imaging of gold and glass structures under artificial aberrations. (a) Main components of AO THG microscope. DM, deformable mirror; L, lenses; X and Y, galvanometers; PMT, photomultiplier tube. (b) Lateral and axial THG images of a 150-nm-diameter gold bead, under 1,300-nm excitation, before and after system aberration correction. (c) Signal profiles along pink and orange lines in (b). (d) Corrective wavefront. (e) Axial THG images of the glass-air interface inside a capillary tube (objective correction collar set to zero), without AO correction and after running the aberration measurement a total of 4 iterations. 24-fold digital gain was applied to No AO image to increase visibility. Yellow asterisk indicates the location of aberration measurement. (f) Signal profiles along the purple and gray lines in (n). (g) Axial FWHM of line profiles taken on AO image in (n) (green circles) and THG signal improvement (AO/No AO, blue asterisks) as a function of the position X. (h) Corrective wavefront in (e). Grayed-out regions indicate broken mirror segments at the time of experiment. Post-objective power: 1 mW in (b), 3 mW in (e). Scale bars, 1 μm in (b), 50 μm in (e)..... 31

Fig. 3.7 AO improves THG in vivo imaging of *B. distachyon* root tissues. (a) Schematic showing the EcoFAB growth chamber used for imaging the roots of *B. distachyon*. Note that the EcoFAB is inverted for imaging. (b) Lateral THG images of the mature zone of a *B. distachyon* root, under 1,300 nm excitation, without and with AO. Ratio of the averaged THG signals within the yellow ovals in (a,b,e,h,i) is indicated. Post-objective power: 2.2 mW. (c) Zoomed-in views of the area in the dashed box in (b). (d) Signal profiles along the orange and green lines in (c). (e) Axial THG images along the dashed line in (b) acquired without and with AO. Post-objective power: 2.7 mW. (f) Signal profiles along the purple lines in (e). (g) Corrective wavefront. Scale bars, 50 μm. 32

Fig. 4.1 Optical setup for the third harmonic generation microscopy with homodyne detection. M-HWP: motorized half-wave plate; PBS: polarized beam splitter; HWP: half-wave plate; L1 and L2: focusing lenses; C1 and C2: BBO crystals; GBP: colored glass bandpass filter; GLP: Glan laser polarizer; BD: beam dump; EOM: electro-optic modulator; CHP: optical chopper; DS: delay stage; Di: dichroic mirror; X and Y: galvanometric scanning mirrors; SL1, SL2 and SL3: scan lenses; TL: tube lens; 50:50 BS: 50:50 beam splitter; BP: bandpass filter; PMT: photo multiplier tube. 39

List of tables

Table 2.1 Signal gains after AO at two pinhole sizes 13

Acknowledgments

My dream of becoming a scientist was deeply rooted in the influence of my grandfather, a bridge engineering professor. He was proud to be an intellectual in his time in China, standing firmly by his values, integrity, and passion for making a meaningful impact on society. When I began my journey to the United States for my Ph.D. in 2018, he often shared his dream of flying over to attend my graduation with excitement. My grandmother, too, loved me deeply. Even as she grew older and her mind began to fade, she continued to care for me, checking in from time to time to see if I was doing well alone in a foreign country, and asking—although long after the Spring Festival, as she lost track of the time—if I had eaten dumplings to celebrate. Although they never had the chance to visit the United States, they loved and supported me unconditionally in their own ways. Sadly, they both passed away three years ago. I have never been able to see them again due to the distance, the pandemic, and the visa policies since 2018. I was fortunate to say my final goodbye via video calls, and I still see them and talk to them in my dreams. Grandma and Grandpa, I hope I have made you proud. This thesis is dedicated to you.

I joined Prof. Na Ji's lab in 2019 with limited hands-on experience in both optics and experimental research. It was Na who made me realize that diving in and getting my hands dirty is the only way to truly learn and build something of my own. She also taught me that being rigorous and thinking based on data are the qualities a physicist should have, and that a strong sense of ownership over a research project is the lasting and effective drive behind meaningful progress. Through her mentorship, I developed both solid knowledge and practical experience in optics and microscopy, equipping me to be a competent Doctor of Philosophy and to confidently lead independent projects as I begin my next journey as a postdoc.

Over the past five and a half years in Ji lab, I've been incredibly grateful to have had such amazing labmates and mentors. Dr. Qinrong Zhang, my first mentor, was always kind, patient, and supportive. She was not only a reliable senior scientist but also a trusted friend. Her diligence, pursuit of excellence, and warm attitude toward her mentees made her a role model I will always look up to. I was equally fortunate to have Dr. Cristina Rodríguez as my second mentor, who introduced me to the field I am in now. Her well-rounded expertise in science and communication set a standard I strive to meet, and her support during my postdoc search meant so much to me. I'd also like to give a big shout-out to Dr. Jun Zhu, Dr. Katharine Borges, and Hyeonggeon Kim. Although we didn't collaborate extensively in research, our science discussions were always enjoyable, and I'm especially grateful for their generous sharing of experiences, insights, and hands-on help during my postdoc search. Moreover, I truly couldn't have asked for a better PhD mentee than Umaima Afifa, who is talented, engaged, resourceful, and made my last half-year in the lab even more rewarding. My heartfelt thanks also go to all the other Ji lab members and collaborators, past and present, whose contributions have enriched my journey and made my time here a truly great learning experience.

Over this journey, I have shared countless life moments with my precious peers. In addition to my labmates, Jerry, Xingzhi, Zhibo, and Zihan have been important people in my PhD life from nearly the beginning of this path. Together, we experienced so many rich moments—joy and sorrow alike—and provided each other with unwavering support.

I also cherish my encounter with Alanna, Zhouyan, Marshall, Yuning, Chloe, and Weiran, whom I met through the Datong Society, a student community I deeply value, and with them, I found a sense of togetherness that I truly treasure; Daren, Yunbo, and Jiayi are also dear friends I made or reconnected with during my time at Berkeley, with whom I shared so many meaningful and memorable moments. These are my trusted companions. Beyond our intellectual engagement and shared values and passions, we also created wonderful memories celebrating life and the things we love.

Earning a PhD and being trained to become an independent scientist has been anything but easy for me. Arriving at the other end of the tunnel, I feel immense gratitude for the love and support I received from all my friends. I want to give special shout-outs to Qinrong, Alanna, Zhouyan, Daren, Yunbo, and Weiran. Throughout my struggles and indecision—wavering between career paths and not deciding to continue my academic life until the final half year of my program—it was you who stood by me during the tough times, listened to my struggles, supported every decision I made, and shared in my happiness and sadness. I know it has been a lot to ask, and I feel incredibly blessed to have you here, celebrating this milestone with me as I earn my Ph.D. Your presence made my Ph.D. life complete.

Over the years, Berkeley has become a place to which I feel deeply connected. It has taught me far more than just academics. It is a public university with students of diverse backgrounds. Meanwhile, many students and faculty here view the world as an imperfect place and fight for a better one as engaged members of the community. Not only have I learned by witnessing students' involvement in campus, social, and global issues, but I have also learned through teaching physics at this public university. In doing so, I've gained insight into how to be a better educator for my students coming from varied backgrounds, and it has been incredibly rewarding to see them overcome both the challenges of the course and their own personal barriers. One of the most meaningful moments was receiving a signed T-shirt from my students, filled with their heartfelt blessings and personal messages as a token of their appreciation. Moreover, I've come to realize that not everyone in society has been given the same opportunities for success—there are significant barriers. For starters, not everyone has had the encouraging environment for pursuing a physics major that I've been fortunate enough to experience, as gender bias in one's upbringing can prevent some from even dreaming of such paths.

In the end, I would like to thank the most important people in my life, my parents. Their love for me is truly unconditional. Even though I am overseas, the time difference and distance may have separated us, but our bond has never weakened. I love you always.

As is often quoted in theses, I've just come to realize that "graduation from a PhD is not the end but the beginning of a brand-new journey." I am deeply privileged to have had all of you accompany me on this path, and I hope our paths will cross again. The mountains are high, and the waters are long, but our bond is as enduring as they are.

Chapter 1

Introduction

1.1 Optical sectioning microscopy

Optical microscopy has become an essential tool across many fields, including biological sciences, due to its ability to visualize the microscopic world[1]. A key challenge in conventional widefield microscopy arises when imaging thick samples—illumination light passes through the entire sample thickness, and the resulting signal light from both above and below the focal plane of the microscope objective is collected indistinguishably along with the in-focus signal. As a result, the out-of-focus features obscure in-focus details, thereby reducing image resolution and contrast[2]. In contrast, microscopes with optical sectioning capability are able to capture clear images of thin slices inside thick samples with minimal signal contamination from other planes. This capability also allows for 3-dimensional visualization of the sample by translating the focal plane across the imaging volume. Highly valuable and widely used in practice, several microscopy modalities that can achieve optical sectioning have been developed, each suited to different application scenarios.

Confocal fluorescence microscopy is currently one of the most popular optical sectioning techniques for fluorescence imaging[2]. To eliminate the excessive background emission caused by fluorescent molecules excited throughout the illuminated thickness by single-photon absorption, the confocal microscope incorporates a detection pinhole conjugated to the focus, allowing in-focus fluorescence photons to be collected while rejecting out-of-focus light[3]. By scanning the focal spot and collecting the fluorescent signal point by point, it forms a high-contrast, high-resolution image of the focal plane with minimal out-of-focus blur. Biologists have been using confocal microscopy to image three-dimensional fluorescent samples, including fluorescent-labeled cultured cells, tissue slices, and intact biological tissues[2,3]. Although the confocal pinhole provides depth-resolving power in thick samples, imaging depth remains constrained by light scattering and absorption. Depth penetration of confocal microscopy typically reaches tens to around 100 μm in opaque biological tissues, depending on the desired resolution and sample conditions[4,5].

With reduced scattering enabled by near-infrared (NIR) excitation, several nonlinear optical microscopy modalities have been applied for deep tissue imaging in both fluorescently labeled and unlabeled biological samples[6]. Since the signal is generated through a nonlinear process requiring

the simultaneous absorption of multiple photons, it is confined to the focal region, where the photon density is high enough for the simultaneous absorption to be possible. Compared to single-photon confocal microscopy, nonlinear microscopy approaches optical sectioning through restricting the signal generation process itself to the focal plane, which not only eliminates out-of-focus blur but also minimizes overall out-of-focus photodamage. Among various nonlinear imaging modalities, three-photon fluorescence (3PF) microscopy and third-harmonic generation (THG) microscopy have recently emerged as powerful techniques offering subcellular resolution at millimeter depths in opaque tissues, with the latter one provides means to image samples exempting the need of fluorescent labeling [7,8].

In this thesis, I focus on advancing the techniques and the applications of confocal fluorescence microscopy (**Chapter 2**), as well as 3PF and THG microscopy (**Chapter 3 and 4**).

1.2 Optical aberrations and adaptive optics for confocal microscopy

Due to the wave nature of light, a point object is not imaged as a point but rather as a three-dimensional volume known as the point spread function (PSF), even in an ideal imaging system. As a result, the image formed represents the convolution of the PSF and the object. This ideal system, achieving the tightest focus or the smallest PSF allowed by the Abbe diffraction limit, is referred to as a diffraction-limited system, where all light rays forming the focus intersect at the same point with the same phase to create constructive interference[1]. However, achieving diffraction-limited performance in practice is challenging due to optical aberrations induced by various factors, including imperfections in optics and alignment, optical heterogeneity within the sample, and refractive index (RI) mismatches between the sample and the immersion medium. These factors perturb the optical field, leading to an enlarged PSF and degraded image quality in terms of signal, resolution, and contrast[9]. In most microscopy setups, it is often sufficient to focus primarily on phase distortions of the optical field, commonly known as wavefront aberrations[10].

To overcome these challenges, adaptive optics (AO) offers a powerful solution. AO is a set of technologies designed to actively measure and then compensate for wavefront aberrations[10,11]. While AO was initially designed for astronomy[12], researchers have introduced it into the microscopy field with a variety of methods in performing the aberration measurement[13]. Once the aberrated wavefront is measured, a wavefront shaping device, such as a deformable mirror (DM) or a spatial light modulator (SLM), is used to generate an opposite corrective wavefront in order to cancel out the aberration and restore the imaging resolution.

AO methods also vary depending on the imaging modality to which they are applied. In confocal fluorescence microscopy, optical aberrations impact both the excitation and detection paths, requiring corrections in both. By positioning the wavefront-shaping device in the shared path of the excitation and detection light, effective AO can restore a diffraction-limited excitation focus within the sample and a diffraction-limited fluorescence focus at the confocal pinhole, ensuring efficient fluorescence detection through the pinhole.

Several AO methods have been employed in confocal fluorescence microscopy. In **Chapter 2**, this thesis reviews the existing methods, their applicable scenarios, and their limitations. We then introduce an AO method based on frequency-multiplexed aberration measurement, integrated into confocal microscopy, and demonstrate its capability to measure aberrations from fluorescent

features of any size. We also validate that this method can correct large-magnitude aberrations and significantly improve signal, resolution, and contrast for images acquired through and within living zebrafish larvae, as well as of densely labeled neurons in the mouse brain *in vivo*.

1.3 Three-photon fluorescence (3PF) microscopy and third-harmonic generation (THG) microscopy

Conventional single-photon microscopy modalities typically use excitation and emission wavelengths in the visible range. The strong scattering of visible light, primarily due to the heterogeneous bio-tissue components, limits high-resolution optical imaging to thin tissue sections or superficial layers[14]. Three-photon fluorescence (3PF) microscopy[7] and third-harmonic generation (THG) microscopy[15,16] are two nonlinear optical imaging techniques that can overcome this limitation. 3PF utilizes a fluorescence process where three photons are simultaneously absorbed to excite a fluorophore with a shorter emission wavelength, whereas THG is a coherent and energy-conserved optical process that converts three excitation photons into a single photon with exactly 1/3 of the excitation wavelength. The contrast mechanisms of these two modalities are distinct—3PF imaging relies on fluorophores to generate signal, while THG imaging's contrast arises from local optical heterogeneities under tight focusing condition, making it sensitive to variations in refractive indices within the focal volume[17,18]. In other words, THG imaging derives its contrast from intrinsic properties of the sample, making it a broadly applicable imaging modality for acquiring general structural information in a label-free manner. More importantly, the two processes can be employed for imaging simultaneously[8,19], as they share the requirement for high instantaneous intensities from the excitation source, which can be achieved using one femtosecond pulsed laser[20]. Emission signals can be separated by their distinct wavelengths, even when excited by the same source. To achieve emission in the visible range, the excitation light typically needs to be in the NIR domain, which significantly reduces tissue scattering, allowing for deeper penetration[14,21]. Since the simultaneous absorption of multiple photons requires high energy density to achieve sufficient conversion efficiency for detection, the emission is spatially confined to the focal volume, enabling optical sectioning.

The label-free imaging capability of THG is particularly advantageous in scenarios where fluorescent labeling is impractical[22,23]. With non-living samples, we demonstrated THG's capability in imaging micro-architected lattice structures (**Fig. 1.1a,b**)[i] and chemical reactions (**Fig. 1.1c,d**)[ii], showcasing its potential for visualizing non-/low-fluorescing structures with high spatial and temporal resolution. In **Chapter 3**, we demonstrate THG microscopy for *in situ* imaging of plant roots without the need for labeling, highlighting its potential for subcellular resolution structural imaging with significantly improved penetration compared to commonly used single-photon technologies. Simultaneously recorded 3PF signals also enabled us to investigate root-microbe interactions at high spatiotemporal resolution.

---

[i] Manuscript submitted for publication (2024): "Blankenship, B. W., Pan, D., Kyriakou, E., Zyla, G., Meier, T., Arvin, S., Seymour, N., De La Torre, N., Farsari, M., Ji, N., Grigoropoulos, C. P., Multi-photon and Harmonic Imaging of Micro-Architected Materials."

[ii] Manuscript in preparation (2024): "Program reactions in heterogeneous media via phase transformation."

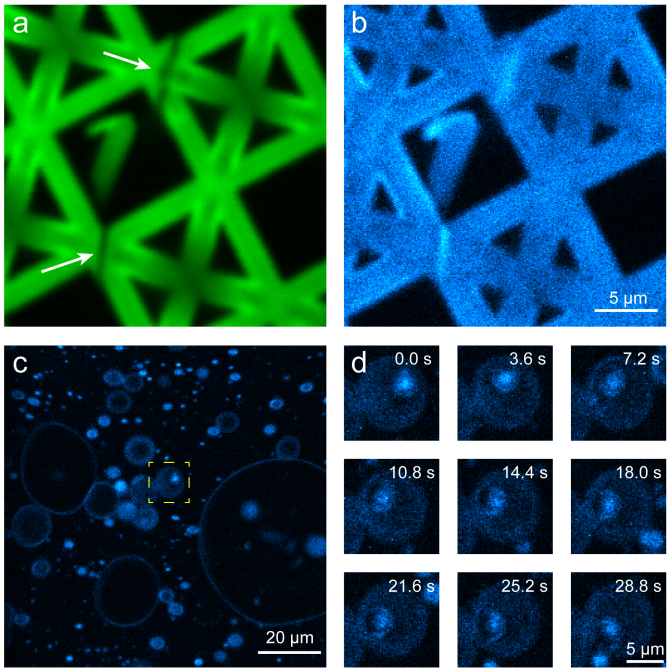

Fig. 1.1 3PF and THG imaging of non-living samples. (a,b) 3PF (green) and THG (blue) images of a periodic micro-additively manufactured lattice structure, fabricated using multiphoton lithography. While THG enables imaging of non-fluorescent structures, the lattice was made from fluorescent materials to allow for side-by-side comparison between the two imaging modalities. Cracks (white arrowheads) were intentionally introduced, visible in the 3PF signal in (a), to demonstrate THG's capability in non-destructive defect examination. As shown in (b), THG provides enhanced contrast at the defect sites due to abrupt changes in refractive index. (c,d) THG imaging of chemical reactions in heterogeneous media via phase transformation, with enhanced contrast at the phase separation boundaries within droplets due to differing optical properties. (d) A zoomed-in view of the yellow box in (c), showing the site of phase separation rotating over 9 consecutive time points.

Similar to confocal fluorescence microscopy, THG imaging suffers from optical aberrations, which affect focus quality and degrade imaging performance[24–26]. This inspired us to apply the aforementioned frequency-multiplexed AO method for aberration measurement and correction. However, the mechanism behind the generation of the THG signal is more complex and distinct from that of fluorescence, making it crucial to experimentally verify the effectiveness of our AO method using the THG signal for aberration measurement. In **Chapter 3**, we also demonstrate that our AO method can successfully measure and correct large aberrations, and we also apply AO to live plant samples. Both demonstrations were performed under label-free conditions, with the THG signal originating from the glass-air interface and the root cell wall, respectively. This work enhances the utility of THG for biological imaging and broadens the application of AO methods.

1.4 Homodyne THG microscopy

THG imaging typically uses a fixed-frequency laser that is far from resonances in the sample, leading to low optical conversion efficiencies[27]. While a higher excitation power P can potentially increase the THG signal following P^3, this requires a delicate balance between the achievable signal level and the photodamage caused by the high excitation power delivered to the sample[28]. In **Chapter 3**, we discuss how the post-objective power levels used for imaging plant roots,

ranging from 2 to 15 mW, provided sufficient signal but also induced photo- and heat-damage to certain root regions. This is a particular concern for long-term imaging, which is a key focus of this project.

Several methods have been proposed to enhance the weak THG signal. Some approaches[29,30] involve fine-tuning the excitation wavelength to match the resonant frequency or the dispersion of a specific structure of interest. However, these methods are not practical for imaging samples with diverse or unknown structures. Optical homodyne detection has emerged as an effective technique for enhancing signal extraction. This method compares the signal with a reference light that shares the same frequency[31]. When applied to THG imaging[28], it takes advantage of the coherent properties of the generated signal. The reference light at the THG signal frequency, pre-generated using the same excitation source, coincides with the original excitation light (the fundamental light) at the sample. Through this process, the interference between the signal and reference enhances the THG signal. In **Chapter 4**, a review of homodyne detection for harmonic generation imaging is provided. I also present a design for THG microscopy with homodyne detection, along with preliminary progress in building such a system. This ongoing project holds the potential to achieve high-sensitivity THG imaging of biological samples, particularly plant roots.

Chapter 2

Frequency-Multiplexed Aberration Measurement for Confocal Microscopy[i]

2.1 Introduction

Widely applied in biology[32], single-photon confocal fluorescence microscopy employs a confocal pinhole to achieve optical sectioning and high-contrast imaging[33]. However, aberrations due to imperfections in optics, alignment, and refractive index mismatches in three-dimensional (3D) samples degrade signal, resolution, and contrast[32,34–36]. Adaptive optics (AO) can improve imaging performance by measuring and correcting aberrations using wavefront shaping devices such as a deformable mirror (DM)[37–40]. Positioning a DM in the common path of excitation and emission light, AO can simultaneously correct for aberrations in both light paths, ensuring a diffraction-limited excitation focus and efficient detection of the fluorescence through the confocal pinhole.

Several AO methods have been employed in confocal fluorescence microscopy. Direct wavefront sensing methods measure wavefront distortion of fluorescence emitted by 3D-confined "guide stars", such as implanted beads or sparsely-labeled fluorescent structures, with a wavefront sensor[41,42]. In more densely labeled samples, a confocal pinhole before the wavefront sensor blocks out-of-focus light from contaminating wavefront measurement[43,44] but spatially filters the wavefront and reduce accuracy[45]. A pulsed laser can create a 3D-confined two-photon fluorescent guide star[46,47] but substantially increase system cost. All direct wavefront sensing methods require precise calibration and alignment of wavefront sensors, adding complexity to the microscope. In contrast, indirect wavefront measurement does not require a wavefront sensor. Modal-based methods measure aberration by introducing known wavefront distortions and measuring their effects on image quality[48]. Applied to confocal fluorescence ophthalmoscopy[49], a pupil-segmentation-based method determines the slopes of individual wavefront segments by measuring image shifts with different segments illuminated[50]. This method works with 2D and sparsely

[i] Adapted from "Pan, D., Ge, X., Liu, Y. T. et al. Frequency-multiplexed aberration measurement for confocal microscopy. *Optics Express* 32, 28655–28665 (2024)."

labeled 3D samples[51], but not densely labeled 3D samples[52] due to the reduction of excitation NA when only a single pupil segment is illuminated.

Previously, we developed a frequency-multiplexed variant of the pupil-segmentation approach for multiphoton fluorescence microscopy[8,53,54]. In this method, the entire pupil is illuminated during aberration measurement, which maintains high excitation NA thus can be applied to densely labeled samples. In this work, we utilized the same principle for single-photon confocal microscopy. Measuring aberration from fluorescent features of any size and correcting large-magnitude aberrations, our method substantially improved signal, resolution, and contrast, including for images acquired through and within living zebrafish larvae as well as of densely labeled neurons in the mouse brain *in vivo*.

2.2 Methods

2.2.1 AO confocal fluorescence microscope

The optical path of our AO confocal fluorescence microscope is shown in **Fig. 2.1a**. The 660-nm excitation light (IBEAM-SMART-660-S, TOPTICA Photonics) reflected off a dichroic mirror (Di: Di03-R660-t3-25x36) and a segmented DM with protected silver coating (Hex-111-X, Boston Micromachines). The DM was conjugated to a pair of galvanometer scanners (X, Y: 6215H, Cambridge Technology) and the back pupil plane of a water-dipping objective (Olympus XLPLN25XWMP2, 25× NA 1.05) using three lens pairs (L1-L6: AC254-400-B and AC254-300-B; SL50-2P2 and SL50-2P2; SL50-2P2 and TTL200MP; Thorlabs). The optics for AO (i.e., DM, L1, and L2) had an estimated light throughput of >95% at the fluorescence emission band, whose inclusion thus led to insubstantial signal loss. Because the image of the DM slightly underfilled the back pupil of the objective, the effective NA of the light modulated by the DM was 0.93. The emitted fluorescence was collected by the same objective and descanned by the galvos. After reflecting off the DM, the fluorescence passed through a dichroic mirror and was focused by a lens (L7: AC254-500-B, Thorlabs), which had the DM located on its front focal plane, onto a confocal pinhole (P100D or P200D, Thorlabs; corresponding to 0.6 or 1.2 airy units (AU)). The light was detected by a photomultiplier tube (PMT: H7422-50, Hamamatsu) after passing through the pinhole and one or three emission filters (LP02-671RU, Semrock; or ET700/50m, Chroma; FF01-732/68-25, Semrock; FF01-708/75-25, Semrock). As the excitation and emission light shared most of the light path and were both reflected by the DM, the DM was able to correct for aberrations in both paths.

2.2.2 Frequency-multiplexed aberration measurement and correction

The frequency-multiplexed aberration measurement[53] determines the tip/tilt correction and phase offset required in order for each beamlet reflected off a DM segment to converge to the same focal volume and constructively interfere to form a diffraction-limited focus. In the case of confocal microscopy, DM applies tip/tilt and phase corrections to the wavefronts of both excitation and emission light to form a diffraction-limited excitation focus inside the sample and a diffraction-limited fluorescence focus at the confocal pinhole, respectively.

To find the required tip/tilt for each beamlet, we fixed half of the segments (grey segments, **Fig. 2.1b**) with the beamlets reflecting off these segments forming a stationary reference focus. We then varied the tip/tilt of the other segments (yellow segments, **Fig. 2.1b**) which scanned their corresponding beamlets around the reference focus. The interference between a beamlet and the

reference focus was strongest when they maximally overlap. We measured the interference strength for each beamlet at a specific tip/tilt by modulating its phase (i.e., piston value of the corresponding DM segment) at a distinct frequency (ω_1, ω_2, ..., ω_n, for n modulated segments), Fourier transforming (FT) the signal trace recorded during modulation, and extracting the FT magnitude at the beamlet's modulation frequency ω_k (magenta line, **Fig. 2.1b**).

Repeating for all tip/tilt values, we acquired a 2D map for each beamlet linking applied tip/tilt values to interference strengths (right panel, **Fig. 2.1b**). We then fit each 2D map and applied the tip/tilt values corresponding to peak interference strength to the corresponding modulated segments. Switching the fixed and moving segments and repeating the above steps, we acquired the tip/tilt values that maximized the overlapping of all beamlets.

We then determined the phase offsets following a similar multiplexed modulation procedure[54]. Fixing half of the segments but modulating the phase of the other half, each segment at a distinct frequency, we acquired and then Fourier transformed the signal trace. FT phase values at the modulation frequency ω_k's (orange line, **Fig. 2.1b**) were then added to the corresponding beamlets to ensure constructive interference at the focus. Same procedure was then applied to the other half of the segments to complete phase correction, with the final corrective wavefront displayed by the DM.

A mathematical description of the entire process and a flow chart describing one iteration of aberration measurement can be found in [55].

2.2.3 Practical considerations

Because the excitation laser had a Gaussian illumination profile with lesser intensity at the edge segments, the FT magnitudes from modulating an edge segment were smaller than those from a more central segment. We designed our DM profile to underfill the objective pupil plane (see **Section 2.2.1**), so that the light intensity at the edge segments did not drop as much as it would with a larger DM profile.

Iterations of tip/tilt and phase measurements may be needed to attain optimal correction due to the initially aberrated reference focus. The number of iterations required scaled with the severity of the aberration. Because an individual mirror segment only has tip, tilt, and piston controls, it offers a 2D planar fit to the corrective wavefront. If a large residue aberration remains after the planar fit by the mirror segment, it would decrease the FT magnitude. To boost the FT magnitudes of such segments (typically edge segments), occasionally, we only modulated the few segments that showed poor SNR in the previous iteration, while keeping the majority of segments fixed to increase the FT magnitudes thus measurement sensitivity of the modulated segments. We still consider them as one iteration of aberration measurement, and 5 out of 54 total iterations carried out in experiments described here adopted this approach.

For biological samples, duration of signal acquisition per iteration varied between 10 s and 32 s (depending on the number of modulated segments and the number of tip/tilt values). DM settling time added another 3 – 6 s to measurement time. In some experiments, we removed global tip/tilt and defocus from the corrective wavefront to preserve mirror stroke.

Either 0.6 AU or 1.2 AU pinhole was used for aberration measurement and confocal imaging of different samples. The 0.6 AU pinhole provided better optical sectioning and resolution than the 1.2 AU pinhole but transmitted less signal. Whenever possible, we used the 0.6 AU pinhole. For

samples whose initial fluorescence signal was too low for accurate aberration measurement, either because of large aberration or weak fluorescent labeling, the 1.2 AU pinhole was used.

As our method parks the excitation focus at the same sample location during aberration measurement, we carefully balanced excitation power (thus signal strength) with photobleaching. When necessary, we used the 1.2 AU pinhole to allow more fluorescence to be detected, which enabled us to reduce exposure time and excitation power to further minimize photobleaching. As a result, we observed minimal photobleaching (<5-10% drop in signal) during aberration measurement in most samples, except for miRFP680-labeled neurons described below, for which ~30% photobleaching was observed during the first iteration of aberration measurement. Even for miRFP680, the impact of photobleaching on aberration measurement accuracy was likely low: For each segment, the tip/tilt values were applied in a random order; as a result, photobleaching would increase the noise in the FT magnitudes but would not bias the tip/tilt correction values, which were acquired by fitting the FT magnitude peak with a 2D gaussian. Moreover, in practice, aberration can be measured from fluorescent features of lesser interest (e.g., beads or bright fluorescent cell bodies near the features of interest), preserving the fluorescence of primary interest. Incorporating a fast shutter (e.g., an acousto- or electro-optic modulator) in the AO confocal system to turn off excitation light during dead time of aberration measurement (e.g., DM settling time) would further reduce photobleaching.

2.2.4 Bead and fluorescent solution samples

To prepare beads samples on microscope slides, 0.2-µm-carboxylated dark-red fluorescent bead solution (F8807, Invitrogen) and 4-µm-diameter four-color fluorescent bead solutions (blue/green/orange/dark red, T7283, Invitrogen) were pipetted onto microscope slides (12-550-12, Fisher Scientific) pre-coated with poly(l-lysine) hydrobromide (10 mg/mL; Sigma-Aldrich, P7890).

To prepare the bead-in-capillary-tube sample, 1-µm-diameter four-color fluorescent bead solution (blue/green/orange/dark red, T7282, Invitrogen) was injected into a glass tube (inner/outer diameter: 0.25-0.3 mm/1 mm, 5-000-2005, Drummond) precoated with poly(l-lysine) hydrobromide.

The fluorescent solution sample was prepared by pipetting aqueous solution of Evans Blue (5%, E2129, Sigma-Aldrich) onto a microscope slide and covered with a coverslip (No. 1.5, Fisher Scientific) with a spacer (>1 mm thick) in between. The coverslip-induced aberrations were pre-corrected by adjusting the correction collar of the objective.

2.2.5 Zebrafish preparation and imaging

Treatment of phenylthiourea (0.2 mM) was applied to wild-type zebrafish from 1 day post fertilization (dpf) to prevent pigmentation.

For the experiments that imaged beads through zebrafish larvae, at 3-5 dpf, zebrafish larvae were immobilized with tricaine and mounted laterally with 1-2% low-melting point agarose onto a petri dish (P35G0.17014C.S, MatTek) whose glass bottom was coated with 0.2-µm-diameter fluorescent beads as described previously.

For the experiments that imaged the gaps between the somite near the notochord of the larvae, at 3-5 dpf, we incubated the larvae in Alexa 647 dye solution (15µM, Alexa Fluor) at room temperature for 2-5 hours and washed out with E3 for 2-3 times. The gaps between the somite near

the notochord of the larvae were filled with fluorescent solution after incubation. Subsequently, the larvae were immobilized with tricaine and mounted dorsally with 1.4% agarose onto a petri dish.

2.2.6 Mouse preparation and imaging

Wild-type mice (C57BL/6J) were used for *in vivo* brain imaging with cranial window implantation. Mice were given the analgesic buprenorphine subcutaneously (0.3 mg per kg of body weight) and anesthetized with 1–2% isoflurane by volume in O2 during surgery. A 3-mm craniotomy was performed. Virus injection was also performed using a glass pipette back-filled with mineral oil, which injected 300 nL of AAV-CaMKII-miRFP680[56] (9×10^{12} vg/mL) at 250 µm below cortical surface at each injection site. A cranial window made of a glass coverslip (No. 1.5, Fisher Scientific) was embedded in the craniotomy and sealed in place with Vetbond (Vetbond, 3M). A titanium

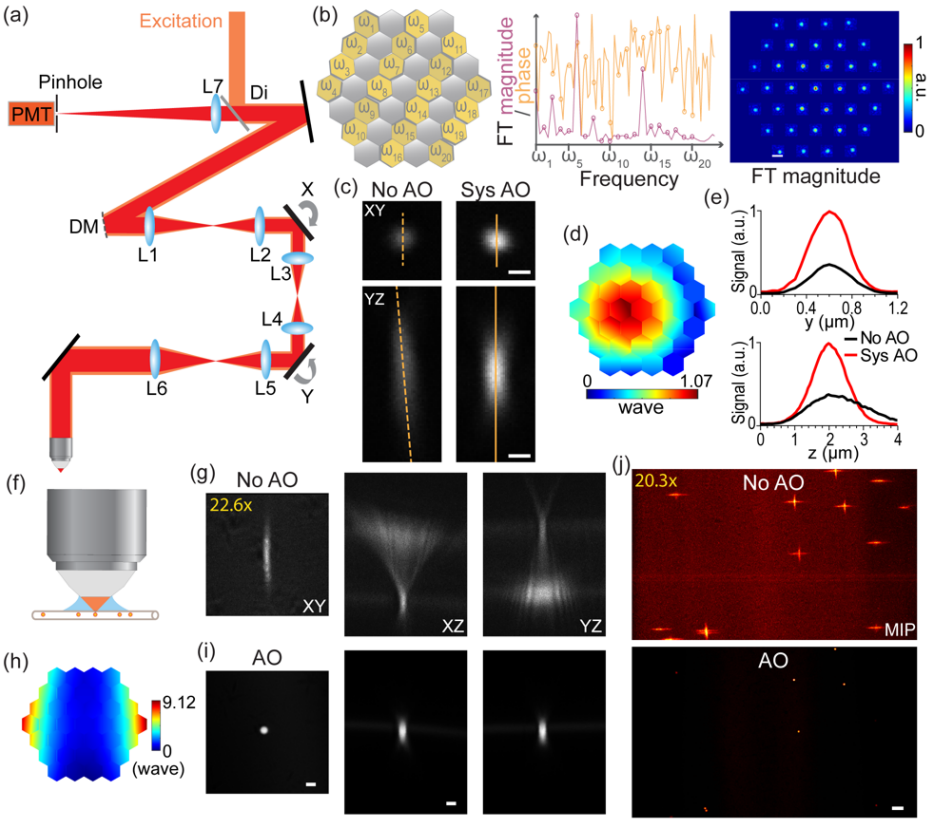

Fig. 2.1 AO confocal fluorescent microscopy. (a) Schematics of microscope. (b) Frequency-multiplexed aberration measurement. Left: DM divided into modulated (yellow) and fixed (grey) segments. Middle: FT magnitude (magenta) and phase (orange) of example signal trace from tilt and phase measurement, respectively. Right: 2D FT magnitude vs. tip/tilt maps of all DM segments. (c) XY and YZ PSFs measured with a 0.2-µm-diameter bead before and after system AO correction. (d) Corrective wavefront for system aberration. (e) Lateral and axial signal profiles along yellow lines in (c). (c)-(e) 0.6 AU pinhole. (f) 1-µm-diameter fluorescent beads in a capillary tube. (g) XY, XZ, YZ images of a 1-µm-diameter bead before AO correction. (h) Corrective wavefront. (i) XY, XZ, YZ images after AO correction. (j) Maximum intensity projection (MIP) of a 25-µm-thick image stack over 250-µm × 150-µm field of view before and after AO, respectively. (f)-(j) 1.2 AU pinhole. 22.6× and 20.3× digital gains for No AO images in (g,j), respectively, to increase visibility. Scale bars: Right panel in (b) 10 µm, (c) 0.5 µm, (i) 2 µm, (j) 10 µm. Post-objective power for aberration measurement: (c)-(e) 0.9 µW, (f)-(j) 0.3-3.9 µW; for image acquisition: (c) 3.2 µW, (g)-(j) 1.9 µW.

headpost was attached to the skull with cyanoacrylate glue and dental acrylic. Neurons expressing miRFP680 were imaged 4 weeks after the virus injection. During imaging, the mouse was head-fixed and under anesthesia with isoflurane (1–2% by volume in O2).

2.2.7 Animal experiments

All experiments involving animals were approved by the Animal Care and Use Committee at the University of California, Berkeley.

2.3 Results

2.3.1 System aberration correction of the confocal fluorescence microscope

We first assessed the performance of our frequency-multiplexed aberration measurement method on correcting the system aberration in our microscope. Using the procedures described in **Section 2.2.2**, we measured and corrected the system aberration with 0.2-μm-diameter fluorescent beads at a post-objective power of 0.9 μW. We then measured the lateral and axial point spread functions (PSFs) before and after system aberration correction using a 0.2-μm-diameter fluorescent bead **(Fig. 2.1c**). Applying the corrective wavefront (**Fig. 2.1d**) on the DM increased the bead's fluorescence signal by 2.6 times and improved its axial full width at half maximum (FWHM) from 2.0 μm to 1.2 μm, while the measured lateral FWHM stayed the same at 0.4 μm (**Fig. 2.1e**). Both the lateral and axial FWHM after system aberration correction were close to diffraction-limit performance (0.3 μm and 1.4 μm for calculated lateral and axial FWHM at 0.93 NA and 0.6 AU pinhole, respectively), indicative of effective correction for aberrations in both excitation and detection paths. All ensuing experiments started with the system aberration already corrected and all images labeled with "No AO" were acquired with system aberration correction.

2.3.2 Correction of large aberrations induced by a capillary tube

We then tested our method's capability in measuring and correcting large sample-induced aberrations. To this end, we imaged 1-μm-diameter fluorescent beads attached to the inner wall of a glass capillary tube (**Fig. 2.1f**). The mismatch in refractive indices between the objective immersion medium (i.e., water) and glass, together with the strong curvature of the glass capillary introduced severe aberrations, yielding highly distorted lateral and axial images of the beads (**Fig. 2.1g**). After 5 iterations of aberration measurements (with 13.1×, 1.3×, 1.4×, 0.96×, and 1.04× signal increase per iteration), we obtained a large-amplitude corrective wavefront dominated by astigmatism (9.1 waves peak-to-valley; **Fig. 2.1h**), which led to a 22.6× increase in peak signal and drastically improved lateral and axial resolution (**Fig. 2.1i**). For this sample, the corrective wavefront acquired near the center of the imaging field of view was effective in improving images of the beads distributed over the diameter (~250 μm) of the capillary tube (**Fig. 2.1j**).

2.3.3 Adaptive optical correction of artificial aberrations using different feature sizes

Introducing four artificial aberrations by displaying Zernike modes of astigmatism, coma, spherical aberration, or trefoil with peak-to-valley value of 1 wave on the DM, we further investigated whether our method can accurately measure aberration using signals of fluorescent features of varying sizes including 0.2-μm-diameter, 4-μm-diameter fluorescent beads, and Evans Blue fluorescent solution through a 0.6 AU confocal pinhole. We plotted the signals of the three

features as well as the axial FWHMs of both bead samples before and after iterations of AO (**Fig. 2.2**). For both bead samples and all four aberrations, one iteration of aberration correction led to substantial signal increase: In all but one cases, bead signal recovered to >90% of the aberration-free signal (~80% for coma with a 4-μm-diameter bead). Three iterations of aberration correction completely recovered their signals. Axial FWHM showed a similarly fast convergence with one or at most two iterations required to achieve diffraction-limited performance.

Consistent with previous findings in multiphoton microscopy[8,51], signal of smaller features was more severely reduced by aberration than that of larger features. Consequently, AO improved the signal of the 0.2-μm-diameter beads (by 3.1×, 4.8×, 3.9×, 2.7× for astigmatism, coma, spherical aberration, and trefoil, respectively) more than that of the 4-μm-diameter beads (by 1.7×, 1.9×, 2.1×, 1.6× for astigmatism, coma, spherical aberration, and trefoil, respectively), indicating that aberration correction is crucial for confocal microscopy to acquire images of fine structures in complex tissues. AO also substantially increased fluorescent solution signal (by 1.3 – 1.8×).

Often, fewer iterations were required to reach optimal correction when signal from smaller structures was used for aberration measurement. This can be understood using the following physical picture. An aberrated confocal focus has a larger volume and reduced intensity than an ideal aberration-free focus. Signal from a small object (e.g., 0.2-μm-diameter bead) located at the center of the focus was determined by the peak intensity of the focus. Consequently, it was strongly modulated during multiplexed aberration measurement. In contrast, signal from a large object (e.g., fluorescent solution) was integrated from the entire PSF volume. It is less strongly modulated and requires more iterations to reach the ideal performance.

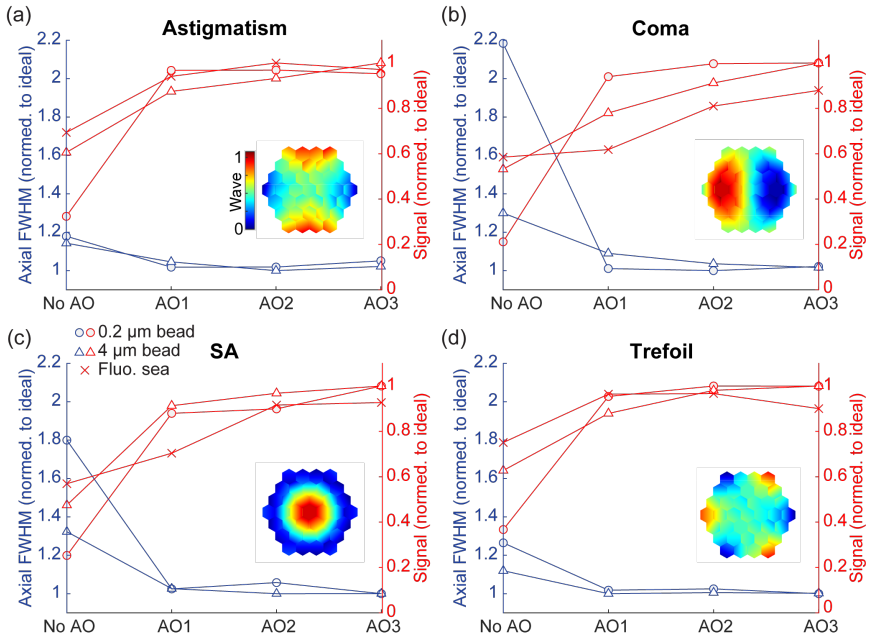

Fig. 2.2 Performance of frequency-multiplexed measurements of artificial aberrations using signal of 0.2-μm-diameter beads, 4-μm-diameter beads, or fluorescent solution, respectively. (a)-(d) Axial FWHM (normalized to aberration-free axial FWHM, blue curves, left axis) for two bead samples and signal (normalized to aberration-free signal, red curves, right axis) versus AO iteration number. Insets: applied artificial aberrations. (a) Astigmatism; (b) Coma; (c) Spherical aberration (SA); (d) Trefoil. 0.6 AU pinhole size. Post-objective power for aberration measurement: 0.2 μW-0.7 mW.

We further compared how pinhole size impacted the gain in signal strength after aberration correction by repeating the above bead experiments with a 1.2 AU pinhole. With aberration, the fluorescence emission light profile at the confocal pinhole is enlarged. With a larger pinhole, more of the aberrated fluorescence light is able to reach the detector. As a result, correcting the aberration of the emission light should cause a smaller signal gain with the 1.2 AU pinhole than with the 0.6 AU pinhole. Indeed, this was what we observed: With the 1.2 AU pinhole, AO improved the signal of the 0.2-μm-diameter beads by 2.6×, 3.0×, 2.6×, 2.0× for astigmatism, coma, spherical aberration, and trefoil, respectively. In contrast, the gain with the 0.6 AU pinhole was 3.1×, 4.8×, 3.9×, 2.7× for the same aberrations, respectively. The same trend held for 4-μm-diameter beads as well (**Table 2.1**), indicating that aberration correction for the emission path is necessary for high-resolution confocal microscopy.

Table 2.1 Signal gains after AO at two pinhole sizes

Experiment\Pinhole size		0.6 AU	1.2 AU
0.2-μm-diameter bead	Astigmatism	3.1×	2.6×
	Coma	4.8×	3.0×
	Spherical aberration	3.9×	2.6×
	Trefoil	2.7×	2.0×
4-μm-diameter bead	Astigmatism	1.7×	1.4×
	Coma	1.9×	1.5×
	Spherical aberration	2.1×	1.7×
	Trefoil	1.6×	1.4×

The same trend of larger signal gains for smaller features persisted: At 1.2 AU, AO improved the signal of the 4-μm-diameter beads by 1.4×, 1.5×, 1.7×, 1.4× for astigmatism, coma, spherical aberration, and trefoil, respectively, less than for 0.2-μm-diameter beads.

Together, these results indicate that our method is capable of accurately measuring aberration using fluorescent features of any size and recovering diffraction-limited imaging performance, with aberration correction being especially important for high-resolution imaging of fine features.

2.3.4 AO correction of biological sample-induced aberrations in vivo

Finally, we applied our AO method to correcting aberrations introduced by live biological samples.

First, we imaged 0.2-μm-diameter fluorescent beads through the body of an immobilized live zebrafish larva mounted laterally, which severely distorted the images of beads underneath (**Fig. 2.3a**). During aberration measurement, we could not determine the corrective tip/tilt for beamlets propagating through the larval notochord, due to the lack of detectable interference between these beamlets and the reference focus (e.g., red boxes, **Fig. 2.3b**). However, previously with the same frequency-multiplexed method, aberration measurement for two-photon excitation light through notochord did not exhibit such difficulty (Supplementary Fig. 4 in [57]). Given that the main difference was the absence of a confocal pinhole in two-photon fluorescence detection, we speculated that the highly curved notochord severely distorted the wavefront of some fluorescence

beamlets, causing too few photons to pass through the confocal pinhole and preventing tip/tilt correction for these wavefront segments. This hypothesis was supported by aberration measurements on a 1-µm-diameter fluorescent bead attached to the inner wall of a glass capillary tube using two different pinhole sizes (Supplementary Fig. 2 in [55]), where improved interference strengths were observed for strongly aberrated beamlets when a larger pinhole size was used during aberration measurement. Nevertheless, even without correcting all segments, the corrective wavefront (**Fig. 2.3c**) substantially improved bead brightness and image resolution (**Fig. 2.3a**; also see the spatial frequency space in insets of **Fig. 2.3a**). For an example 0.2-µm-diameter bead (**Fig. 2.3d**), the lateral and axial FWHMs after AO were 0.6 and 2.1 µm, respectively, larger than the diffraction-limited values when all segments were corrected (**Fig. 2.1c**, 0.4 and 1.2 µm,

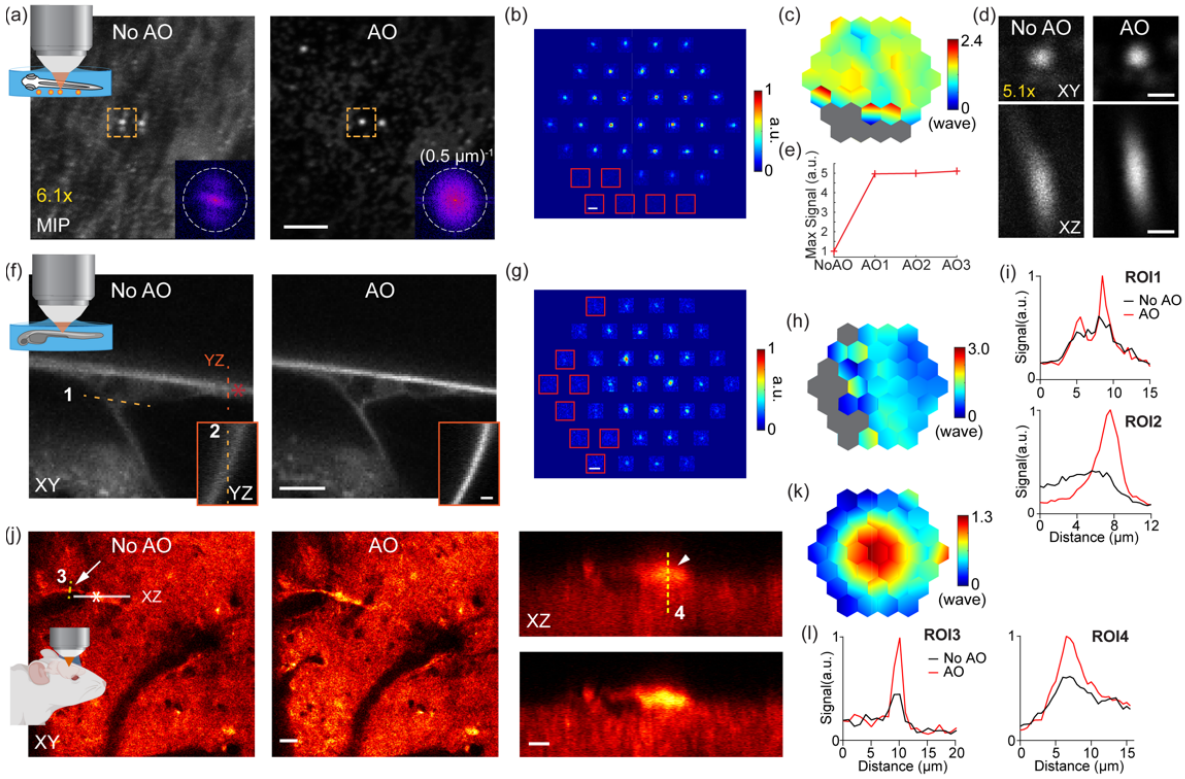

Fig. 2.3 AO improves confocal imaging quality by correcting biological-sample-induced aberrations. (a) MIPs of a 6.25-µm-thick image stack taken without and with AO when imaging 0.2-µm-diameter fluorescent beads through a zebrafish larva. Insets: spatial frequency space representations; dashed circles: (0.5 µm)-1. AO was performed on the bead in the orange box. (b) FT magnitude vs. tip/tilt displacement maps from 1st iteration of AO. (c) Corrective wavefront for (a). (d) XY and XZ images of the bead in the orange boxes in (a) without and with AO. (e) Peak signal of the bead in (d) over iterations. (f) XY images of Alexa 647-labeled somite outlines of a zebrafish larva without and with AO. Insets: YZ images along the red dashed line. (g) FT magnitude vs. tip/tilt displacement maps from 4th iteration of AO. (h) Corrective wavefront for (f). (i) Signal profiles along the dashed lines 1 and 2 in (f). (j) XY images of miRFP680-labeled neurons and XZ images along the white line acquired without and with AO. (k) Corrective wavefront for (j). (l) Signal profiles along the dashed lines 3 and 4 in (j). (a-e, j-l) 0.6 AU pinhole. (f- i) 1.2AU pinhole. 6.1× and 5.1× digital gains for No AO images in (a) and (d), respectively, to increase visibility. Red boxes in (b, g): segments without measurable interference magnitudes. Scale bar: (a) 5 µm, (b) 10 µm, (d) 1 µm, (f) XY images, 10 µm; insets, 2 µm, (g) 10 µm, (j) XY images, 20 µm; XZ images, 5 µm. Post-objective power for aberration measurement: (a- e) 0.5-2.1 µW, (f- i) 2.7-3.3 µW, (j- l) 16-17 µW; for image acquisition: (a, d) 1.2 µW, (f) 3.3 µW, (j) 16 µW.

respectively). Still, one iteration of AO led to a 5.1× signal gain (**Fig. 2.3d**), with additional iterations increasing signal minimally (**Fig. 2.3e**).

Subsequently, we corrected aberrations in a dorsally mounted live zebrafish larva. After incubation in Alexa 647 dye solution, gaps between the somite near the notochord of the larva were filled with fluorescent solution. We measured the fish-body-induced aberration after four iterations of aberration measurements (at asterisk, **Fig. 2.3f**). Similar to above, wavefront segments through the notochord did not give rise to detectable interference (**Fig. 2.3g**). Nevertheless, our partial correction of the excitation and emission wavefronts still led to substantial improvement in image quality (**Fig. 2.3f**). Two nearby gaps were only resolvable after aberration correction (ROI1, **Fig. 2.3f,i**). The fluorescence signal of a thicker gap showed substantial improvement, with its axial image displaying a 2.4× increase in brightness (ROI2, **Fig. 2.3i**) and markedly enhanced sharpness (insets of **Fig. 2.3f**) after AO correction.

We next conducted AO confocal microscopy imaging of neurons through a cranial window in the mouse brain *in vivo* (**Fig. 2.3j**). Cortical neurons were densely labeled with a near-infrared (NIR) fluorescent protein miRFP680[56] by virus transfection. Three iterations of aberration measurements were performed on a cell body (asterisk, **Fig. 2.3j**), resulting in a corrective wavefront (**Fig. 2.3k**) that substantially improved image quality of neuronal features. For instance, a dendrite (arrow, **Fig. 2.3j**) became more visible after AO, with a signal increase of 2.2× (ROI3, **Fig. 2.3l**). A cell body (arrowhead, **Fig. 2.3j**) had a 1.6× increase in signal and its axial image became more confined (ROI4, **Fig. 2.3l**). In both lateral and axial imaging planes, fine features were more easily resolved after AO correction (**Fig. 2.3j**).

2.4 Discussions and conclusions

In this work, we incorporated an AO approach based on frequency-multiplexed aberration measurement into single-photon confocal fluorescence microscopy. Correcting optical aberrations experienced by both the excitation and the emission light, our method substantially improved the signal, resolution, and contrast of images of both nonbiological and biological samples.

Previous demonstrations of this frequency-multiplexed aberration measurement method were in multiphoton fluorescence microscopy, where optical sectioning was accomplished by confinement of nonlinear absorption to within the focal volume and aberration correction was only required for the excitation light. For single-photon confocal fluorescence microscopy, confocal pinhole selectively passes photons emitted from the focal plane while rejecting fluorescence generated by out-of-focus excitation light. As a result, aberrations in both the excitation and emission light paths need to be corrected to achieve diffraction-limited imaging performance. The ability of our aberration measurement to be achieved on fluorescent features of any size, from sub-micron-diameter beads to fluorescent solutions, makes our method generally applicable to a broad range of samples, as we demonstrated in sparsely labeled zebrafish larva and densely labeled mouse cortex *in vivo.*

Chapter 3

Advances in Three-Photon and Third-Harmonic Generation Microscopy for Label-Free Root Imaging[i]

3.1 Introduction

3.1.1 Introduction to multiphoton fluorescence and harmonic generation microscopy

A major challenge for conventional single-photon microscopy is its limited depth penetration. These techniques, typically using excitation and emission wavelengths in the visible range, suffer from strong Mie and Rayleigh scattering by heterogeneous biological tissue components, which restricts high-resolution imaging to thin tissue sections or superficial layers[14]. However, since Rayleigh scattering is wavelength-dependent, near-infrared (NIR) light experiences significantly less scattering than visible light. By exploiting this property, several nonlinear optical microscopy techniques, including multiphoton fluorescence (MPF) microscopy and harmonic generation microscopy, have significantly increased penetration depth, making them valuable non-invasive imaging tools[14,21].

Multiphoton fluorescence microscopy

Unlike single-photon processes, multiphoton excitation involves the simultaneous absorption of multiple photons by the fluorophores to generate fluorescence[58,59]. For example, two-photon fluorescence (2PF) microscopy[6] and three-photon fluorescence (3PF) microscopy[7] are commonly

[i] Adapted from "Pan, D., Rivera, J. A., Kim, P. et al. Label-free structural imaging of plant roots and microbes using third-harmonic generation microscopy. *bioRxiv* (2024). https://doi.org/10.1101/2024.04.13.589377." and "Rodríguez, C., Pan, D., Natan, R. G. et al. Adaptive optical third-harmonic generation microscopy for in vivo imaging of tissues. *Biomed. Opt. Express* 15, 4513–4524 (2024)."

used multiphoton modalities in bioimaging, where two or three photons combine their energy to excite one fluorophore before the latter returns to the ground state and emits a fluorescent photon. Consequently, while the fluorescence emission remains in the visible range[60], excitation wavelengths are typically in the NIR domain, which significantly reduces scattering of the excitation light. Meanwhile, since simultaneous absorption of multiple photons requires high energy density to achieve sufficient conversion efficiency, this process not only necessitates high instantaneous intensities achieved through using a femtosecond pulsed laser[20], but also spatially confines the generation of multiphoton emission to the focal volume. Although emission photons lose spatial information due to scattering, MPF microscopy still detects all photons collected by the objective, assigning the resulting signal to the corresponding focal point before scanning to the next point in the field of view. This point-scanning and detection scheme ensures high detection efficiency while mitigating the scattering effect of the emission light. Together, the scattering challenges associated with the conventional single-photon microscopy are effectively addressed. Additionally, the excitation wavelengths chosen for existing fluorophores also need to avoid ranges with strong absorption by water and blood in tissue[14]. Considering these criteria, 2PF microscopy typically uses excitation wavelengths in the range of 680-1300 nm[60], and 3PF microscopy typically uses wavelengths around 1300 nm and 1700 nm[7,61]. As a result, 2PF microscopy achieves significantly deeper—typically 2 to 3 times greater penetration than the single-photon microscopy when imaging the visible fluorophores, and 3PF microscopy allows for even deeper penetration with its longer NIR wavelengths[21]. In this chapter, 3PF microscopy will be employed to image the autofluorescence (3P autofluorescence) from the structures within the biological tissue *in situ*, with greatly improved penetration compared to the commonly used single-photon technologies.

Harmonic generation microscopy

Harmonic generation is another set of nonlinear optical processes that has been utilized in the optical imaging field. Different from the multiphoton fluorescence process, *n*-th order harmonic generation is a coherent optical process that converts *n* identical excitation photons into one photon having exactly *1/n* of the excitation wavelength[27]. Harmonic generation imaging is essentially a label-free technique as its signal originates from the *n*-th order susceptibility of the medium, exempting the need for fluorescence labeling. While second-harmonic generation (SHG) is generally restricted to imaging non-centrosymmetric structures[62], third-harmonic generation (THG) does not have a specific symmetry requirement. Under tight-focusing condition achieved by an objective with high numerical aperture (NA), THG signal shows high contrast at the locations with local optical heterogeneities (i.e., RI and third-order susceptibility variation) within the excitation focus[15,18,19], making it a valuable tool for acquiring structural information from samples. Additionally, THG imaging can be performed using the same microscopy setup as 3PFM, with its signal collected by the same objective but spectrally separated from the fluorescence signal and detected at an additional channel[8,19], making them complementary imaging modalities that can be simultaneously employed. In biological settings, collagen fibers, cellular and subcellular structures such as membranes, and lipid-rich structures have been imaged with THG microscopy[18]. In this chapter, alongside 3PF imaging, we demonstrate the simultaneous use of THG for *in situ* imaging of biological tissues, specifically plant roots, highlighting its potential for subcellular resolution structural imaging in scenarios where fluorescent labeling is impractical.

3.1.2 Root biology and plant root imaging

Root biology research informs wide-ranging areas of intensifying global interest including soil remediation[63], climate[64], genetics[65], and sustainable agriculture[66,67]. Optical microscopy, capable of visualizing plant morphology at sub-cellular resolution, is critical for understanding plant structure and function[67]. However, compared to more extensively studied plant organs such as stems and flowers, a dearth of imaging studies on plant roots has resulted in roots being continually designated the "hidden half" of the plant body[68].

The native environment of plant roots, composed of soil and organic matters, strongly scatters and absorbs light, severely limiting optical access to plant roots. As an alternative, microfabricated ecosystems such as EcoFABs[69] provide controllable and reproducible growth conditions to plants. The absence of soil in EcoFABs relieves the requirement of uprooting the plant from its growing environment and provides non-destructive optical access for *in situ* imaging of root structure and its immediate microenvironment[70,71].

Single-photon fluorescence microscopy techniques such as confocal microscopy[72] and light sheet microscopy[73–75] have been used to image plant roots[76,77]. However, light scattering by root tissues has limited their applications to relatively transparent or cleared root samples[78]. They also often require the introduction of extrinsic fluorescent labels. Transgenic fluorescent markers are compatible with live root imaging but can only be implemented for plants with established transformation systems and even in the best cases are laborious, whereas vital stains can suffer from poor incorporation[22] or unwanted interference with cellular activity[23]. Thus, a label-free microscopy approach that can image structures at high resolution in opaque live root tissues would be highly desirable but has yet to be demonstrated.

Nonlinear optical microscopy methods utilizing near-infrared excitation light provide greater depth penetration in tissues than single-photon fluorescence techniques, and have been used to image both fluorescently labeled and unlabeled plant tissues[16,79–82]. Two nonlinear imaging modalities, 3PF microscopy and THG microscopy, have recently emerged as a powerful technique to image subcellular resolution at millimeter imaging depths in opaque tissues such as the mouse brain[7,8]. Here, we explored the potentials of using 3PF and THG microscopy for label-free *in situ* imaging at subcellular resolution of live plant roots in EcoFABs, including *Brachypodium distachyon*, a monocot grass known for its genetic tractability and relevance to agricultural crops[83,84], and the dicot *Arabidopsis thaliana*, a central model organism in plant research[85]. We found that THG provided excellent optical resolution and label-free contrast for a variety of subcellular structures, while 3PF from the intrinsic fluorophores of root cells provided complementary structural information. We were able to visualize root hairs, vasculature, as well as subcellular components of mitotically active and border-like cells. In the optically opaque root of *B. distachyon*, THG microscopy imaged vasculature beyond 200 μm in depth in the mature zone and imaged through the entire 230-μm thickness of a root tip. Furthermore, we combined simultaneous label-free and fluorescence imaging to study root-microbe interactions, including real-time monitoring of *Pseudomonas simiae* dynamics in the vicinity of *A. thaliana* roots at single-bacterium resolution and visualizing the fungus *Trichoderma atroviride* adjacent to *B. distachyon* roots at subcellular resolution.

3.1.3 Adaptive optics for THG microscopy

THG microscopy enables imaging deep within scattering tissues. However, as the imaging depth increases, optical aberrations accumulate in the excitation beam as it propagates through the tissue. These aberrations lead to an enlarged excitation focus, reduced focal intensity, and a consequent decrease in the resolution and signal quality of THG images[24–26].

In **Chapter 2**, we discussed an AO method known as frequency-multiplexed aberration measurement and correction. This method involves a compact AO module that has been successfully integrated into both MPF microscopy[53] and confocal microscopy (**Chapter 2**). Despite the differences in detection optical design, in both modalities, our method uses the fluorescence signal collected by the same PMT used in regular imaging for frequency-multiplexed aberration measurement[86]. And by employing a single high-speed segmented deformable mirror (DM) for both aberration measurement and correction, our AO module achieves rapid aberration measurement, high-power throughput, polarization- and wavelength-independent operation, and easy integration into various microscopes.

In this work, we integrated our compact AO module with a THG microscope, which we refer to as the "AO THG microscope," to enable high-resolution, label-free imaging across diverse samples. The key distinction is that the signal used for aberration measurement is the THG signal intrinsic to the sample, rather than a fluorescence signal. This provides the advantage that neither the imaging nor the aberration measurement process requires fluorescence labeling. To validate the performance of our AO THG microscope, we imaged THG-producing glass interfaces under large artificial aberrations and achieved diffraction-limited imaging performance after AO correction. Taking advantage of the high sensitivity of the THG process to interfaces and thin membranes, along with the NIR excitation wavelengths used here (i.e., 1300 nm), our AO THG microscope enabled label-free, high-resolution *in vivo* imaging in highly scattering biological model systems at depth. In this chapter, we show the improved imaging of key anatomical features in the highly scattering tissues of the *B. distachyon* root.

3.2 Methods and materials

3.2.1 3PF and THG imaging of plant roots

3PF and THG microscopy setup

A simplified diagram of our multimodal (3PF and THG) microscopy is shown in **Fig. 3.1a**. The excitation source (not shown) consisted of an optical parametric amplifier (Opera-F, Coherent) pumped by a 40-W femtosecond laser (Monaco 1035-40-40, Coherent). Opera-F was tuned to generate 1,300 nm output at 1 MHz. A Pockels cell (M360-40, Conoptics) controlled the light power. A homebuilt single-prism compressor[87] was used to cancel out the group delay dispersion (GDD) of the excitation beam path. The excitation laser beam was reflected by two conjugated galvanometric scanning mirrors (6215H, Cambridge Technology) and relayed to the back-pupil plane of a high NA water-dipping objective (Olympus XLPLN25XWMP2, NA 1.05, 25×) by two pairs of scan lenses (SL50-3P and SL50-3P, SL50-3P and TTL200MP; Thorlabs). The objective was mounted on a piezoelectric stage (P-725.4CD PIFOC, Physik Instrumente) for axial translation of the excitation focus. The fluorescence and THG signals were collected by the same objective, reflected by a dichroic mirror (FF665-Di02-25x36, Semrock) and detected by two

photomultiplier tubes (H10770PA-40, Hamamatsu). An additional dichroic mirror (Dm, FF458-Di02-25x36, Semrock) and two filters (FF03-525/50-25 for fluorescence, FF01-433/24-25 for THG; Semrock) were used to split and filter the 3PF and THG signals. Frame rates were 0.2 – 0.6 Hz except for **Fig. 3.4**, which was acquired at 0.03 – 0.08 Hz, and **Fig. 3.5a,b**, which was acquired at 1.1 Hz.

Bead sample

Carboxylate-modified fluorescent microspheres (FluoSpheres™, Invitrogen) were immobilized on poly(l-lysine)-coated microscope slides (12-550-12, Fisher Scientific).

Imaging EcoFAB fabrication

Imaging EcoFAB devices were fabricated as described previously[71]. Negative molds for imaging EcoFAB were 3D printed using a Form2 printer (Formlabs) with clear resin version 4 (Formlabs). EcoFAB design can be obtained from https://eco-fab.org/device-design/. Each EcoFAB device was housed in a magenta box with a vented lid (MK5, with vented lid, Caisson Labs) for autoclave sterilization.

***Brachypodium distachyon* growth conditions**

Brachypodium distachyon line Bd21-3 seeds was used for this study[88]. Seeds were dehusked and surface sterilized in 70% ethanol for 30 s, followed by 50% v:v bleach (with 6.25% sodium hypochlorite chlorine) for 5 min, and rinsed 5 times with sterile milliQ water[71]. Seeds were then arranged on a sterile petri dish containing ½ Murashige and Skoog basal salt media (Caisson Labs) with 1% phytogel (Sigma-Aldrich). Surface sterilized seeds were stratified in the dark at 4 °C for 3 days. Following stratification, seeds were allowed to germinate in a growth chamber at 25 °C at 200 $\mu mol \cdot m^{-2} \cdot s^{-1}$, 16-hr light/8-hr dark. Three Days post germination, seedlings were transplanted into sterilized imaging EcoFABs containing 0.5× MS media with 0.8% phytogel[71]. Following transplantation, plants were grown in the growth chamber for three more days before imaging. All root samples were imaged within the EcoFABs except for **Fig. 3.4**, for which the plant was taken out of the EcoFAB and imaged with its root between two glass coverslips to reduce root tip motion.

***Trichoderma atroviride* culture conditions and inoculation**

Three days post germination, sterile *Brachypodium distachyon* seedlings were inoculated with *Trichoderma atroviride* strain IMI[89] containing nuclear GFP label (H1-GFP) (generously provided by Drs. Catherine Adams and Louis Glass, University of California Berkeley, CA, USA). Fungal spores were grown on PDA plates at 28 °C for 7 days 12/12 night/day cycle to induce sporulation. Spores were then harvested using sterile distilled water and separated from mycelia using a 0.4 micron filter (Pall). Spore concentration was determined using Neubauer chamber and then diluted to a spore suspension of $1x10^6$ spores/ml. Seedlings were soaked in the spore suspension for 2 hours prior to transplanting onto Imaging EcoFABs[90]. Following transplantation, plants continued growing in the growth chamber for two more days before imaging.

***Arabidopsis thaliana* and *Pseudomonas simiae* sample preparation**

Seeds of *Arabidopsis thaliana* Col-0 (stock # CS66818) were obtained from the Arabidopsis Biological Resource Center (Ohio State University, Columbus, OH). Seeds were surface-sterilized by immersion in 70% (v/v) ethanol for 2 min, followed by immersion in 10% (v/v) household bleach containing 0.1% Triton X-100 (Roche Diagnostics GmbH) were stratified in distilled water

at 4°C for 2 days. In this study, we utilized two strains of the root-colonizing bacterium *Pseudomonas simiae*, the non-fluorescently labeled strain *P. simiae* WCS417r and the eGFP-expressing strain *P. simiae* SB642, which has been previously characterized[91]. Both strains were pre-cultured under kanamycin selection (150 $\mu g \cdot ml^{-1}$) in Luria-Bertani medium (Sigma-Aldrich) diluted in 0.5× MS medium containing 2.15 g/L, 0.25 g/L of MES monohydrate (ChemCruz), and buffered to pH 5.7. The pre-cultured bacterial cells were washed twice with 0.5× MS medium and used to inoculate the stratified seeds of *A. thaliana* at an initial OD600 of 0.01 for each strain. The inoculated seeds were sown into agar-filled imaging EcoFAB chamber. The growth medium contained 0.5× Murashige and Skoog basal salt mixture (Sigma-Aldrich), 2.5 mM of MES monohydrate (ChemCruz), and was buffered to pH 5.7 and solidified with 1 wt% SFR agarose (Electron Microscopy Sciences). *A. thaliana* seedlings were grown under 16 h light (140 $\mu mol \cdot m^{-2} \cdot s^{-1}$) and 8 h dark regime at 23 °C for 10-14 days.

Digital image processing

Imaging data were processed with Fiji[92]. We used the 'Green' lookup table for 3PF images and the 'Cyan hot' lookup table for THG images. In **Fig. 3.5b**, the 3PF and THG signals were presented with ‘Green’ and ‘Gray’ lookup tables, respectively. For **Fig. 3.5c,d**, the 3PF and THG signals were presented with ‘Yellow’ and ‘Cyan hot’ lookup tables, respectively. To improve visibility, saturation and gamma of some images were adjusted. For **Fig. 3.5d**, we applied the 'RemoveOutliers' function in Fiji to eliminate hot pixels. We generated three-dimensional projection images (**Fig. 3.1f** and **Fig. 3.4a**) using Fiji's '3D Project' function with ‘brightest-point projection’ and depth cueing set at 100% to 50%.

3.2.2 AO THG microscopy

Microscope description

Fig. 3.6 illustrates a schematic of our custom-built THG microscope, as previously described[53]. In addition to the microscope system described in **Section 3.2.1**, the major difference is an extra deformable mirror (DM) within the excitation path. The DM consisting of 37 individual segments (Hex-111-X; Boston Micromachines Corporation) was conjugated to the pair of galvanometers and to the back focal plane of the microscope objective. The DM image underfilled the back aperture of the objective. A field stop (iris diaphragm; Thorlabs) was positioned at the intermediate image plane between the DM and the X galvo to block light reflected off mirror segments at large tilt angles. For the data presented here, the effective NA was ~0.9, corresponding to lateral and axial resolutions of about 0.6 μm and 2.3 μm, respectively.

Aberration measurement method

The details of our frequency-multiplexed aberration measurement procedure were described previously in **Chapter 2**. In summary, we parked the laser focus at one sample location and used the THG signal from this point for aberration measurement. The pupil was divided into 37 regions, corresponding to the number of segments in the deformable mirror (DM). These 37 DM segments were then split into two groups consisting of alternating rows. The aberration measurement procedure first determines the local phase gradients of the wavefront that need to be added to each DM segment so that the beamlets reflecting off them overlap maximally at the focal plane. This was achieved by forming a stationary reference focus using half of the beamlets, while the remaining half of the beamlets were scanned around this focus by applying varying tip/tilt to their

corresponding DM segments. At each set of tip/tilt values, we modulated the phase or intensity of the scanned beamlets by varying the piston values of or applying a large tilt to the corresponding mirror segments, respectively, each at a distinct frequency of hundreds of Hz, and recorded the variation in the THG signal. If a scanned beamlet overlapped with the reference focus, modulating its phase/intensity would lead to changes in THG signal, with the amount of overlap determined by Fourier transforming the time-varying THG signal trace and extracting the Fourier magnitude at the corresponding modulation frequency. This enabled the determination of the phase gradients required for maximal overlap and interference between the modulated beamlets and the reference focus, thus providing the tip and tilt angles to be applied to the corresponding DM segment. By swapping the stationary and the scanned DM segments and repeating the phase gradient measurement process, we obtained the local wavefront gradients required to converge all beamlets to the same location in the focal plane. With all the beamlets converging at a common location, the subsequent step of the aberration measurement procedure involves measuring the phase offsets of each beamlet that would allow them to constructively interfere at the focus. This is accomplished by following a similar frequency-multiplexed procedure[93].

Because the starting reference focus is aberrated, both the phase gradient and phase offset measurement procedures may be repeated for a few iterations to achieve optimal aberration correction. With the final corrective wavefront applied to the DM, all beamlets of the excitation light converged and constructively interfered at the focal plane, thus achieving diffraction-limited performance for THG microscopy.

Plant root sample preparation

For the *in vivo* plant root imaging experiments, *B. distachyon* seedlings were transplanted into microfabricated ecosystem (EcoFABs) containing 50% MS media and allowed to grow hydroponically[69,71,94]. A glass coverslip was used for the bottom of the EcoFAB so that the roots could be non-destructively imaged. Roots from 3-week-old plants were imaged through a glass coverslip that sealed the bottom of the microfabricated PDMS growth chamber.

3.3 Label-free structural imaging of plant roots and microbes using THG microscopy

3.3.1 THG microscopy provides label-free contrast for plant root structures at subcellular resolution

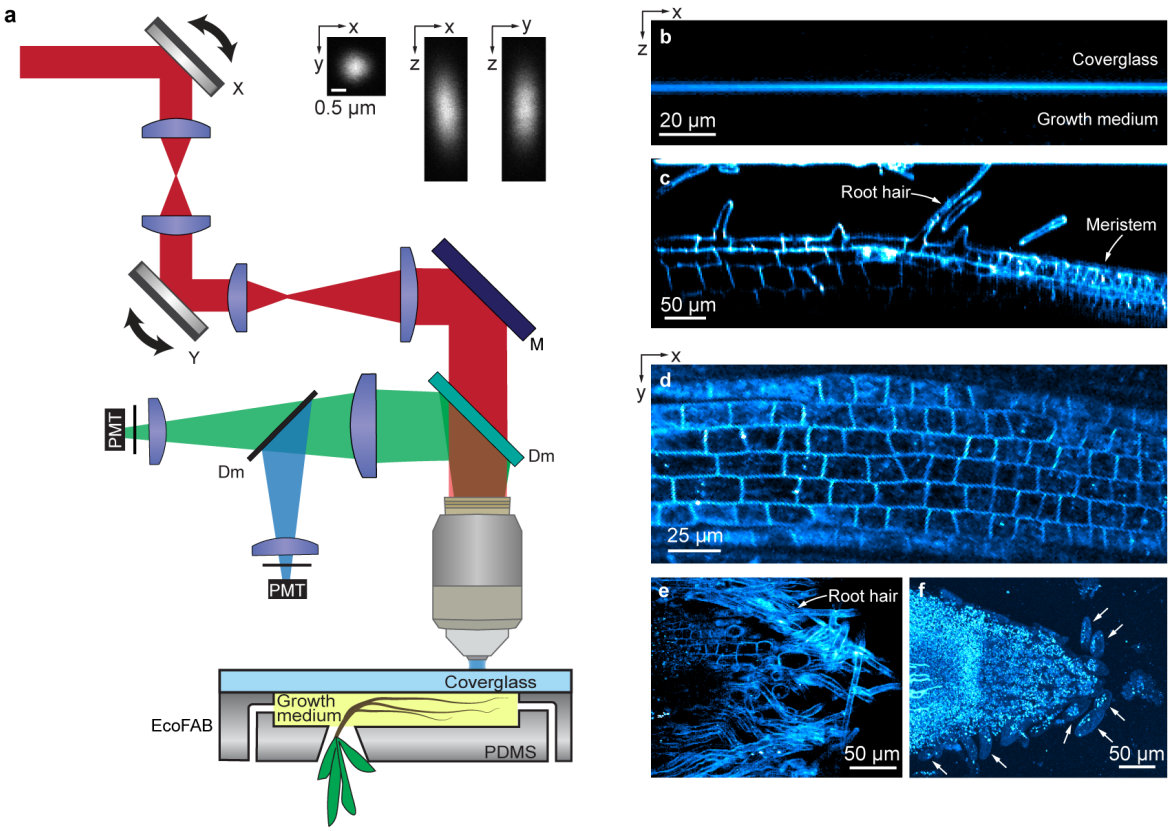

Fig. 3.1 THG microscopy reveals plant root structure at subcellular resolution. (a) Schematics of the microscope and EcoFAB. Red: excitation light; Green: 3P fluorescence; blue: THG. X, Y: X and Y galvanometer mirrors; M: mirror; Dm: dichroic mirror; PMT: photomultiplier tube. Insets: lateral (xy) and axial (xz, yz) images of a 0.2-µm-diameter bead. (b) xz THG image of the interface between coverglass and growth medium. (c) xz and (d,e) xy THG images of *B. distachyon* roots inside the EcoFAB chamber. (b,c) acquired at 2 µm/pixel in X and 1 µm/pixel in Z. (d,e) acquired at 1 µm/pixel. (f) Brightest-spot projection with depth cueing (100% to 50%) of an 88-µm-thick image stack of a root tip acquired at 0.8 µm/pixel and z step size of 2.75 µm. White arrows: border-like cells. Post-objective power: (b) 2 mW, (c,d) 3 mW, (e) 4 mW, (f) 2.4-2.8 mW.

THG, a coherent optical process that can convert three near-infrared excitation photons to one visible photon having one-third the excitation wavelength, has its signal originating from the third-order nonlinear susceptibility[27]. Under tight focusing conditions in microscopy, its contrast derives from the local optical heterogeneities within the excitation focus[15,16,18,95]. When the absorption of three near-infrared photons also promotes a fluorophore to its excited electronic state, 3PF can be generated by the same excitation laser. At longer wavelengths than the third-harmonic signal, 3PF signal can be spectrally separated from and simultaneously detected with the THG signal. The third-order nonlinear excitation involved in THG and 3PF confines the signal generation to within the excitation focus, thus optically sections 3D samples.

We conducted all imaging experiments using a custom-built multimodal microscope[8] capable of simultaneously acquiring THG and 3PF signals (**Fig. 3.1a**). A near-infrared excitation laser beam (λ=1300 nm; Monaco-Opera-F system, Coherent Inc.) propagated through a laser-scanning assembly comprising galvanometric mirrors (X, Y) and scan lenses to overfill a high-numerical-aperture (NA) water-dipping objective (Olympus XLPLN25XWMP2, NA 1.05, 25×). THG at 433 nm and 3PF (500 – 550 nm) signals were separated from the excitation light by a dichroic mirror (Dm) and further separated into two paths by an additional dichroic mirror for detection by photomultiplier tubes. We measured the point spread function (PSF) of our microscope by 3PF imaging of 0.2-μm-diameter fluorescent beads. The PSF had a lateral full width at half maximum (FWHM) of 0.65 μm in the xy plane and an axial FWHM of 1.78 μm (insets, **Fig. 3.1a**).

Seedlings of *B. distachyon* or *A. thaliana* were allowed to germinate within an EcoFAB growth chamber[71] made of coverglass and PDMS before loading into the microscope (Methods). The excitation light entered through the coverglass side of the chamber and the emitted THG and 3PF signals were collected and detected in the epi direction. When the excitation focus was entirely within the coverglass or the growth medium, there was no THG signal generated due to the optical uniformity of the material within the focus[15,27]. When the excitation focus bisected the coverglass-medium interface, a strong THG signal was generated due to the abrupt change of susceptibility from glass to growth medium (**Fig. 3.1b**).

When the excitation focus was scanned across *B. distachyon* roots, THG signal provided high-resolution label-free visualization of various structures in both axial (**Fig. 3.1c**) and lateral (**Fig. 3.1d-f**) planes. Within the root, plant cells appeared as individual compartments with strong THG signal observed at their cell walls, likely due to the different optical properties of the cell wall and the cytopolasm[96,97]. In an example axial (xz) image (**Fig. 3.1c**), we observed elongated cells with root hairs protruding from the root surface – a well-known characteristic of the mature root zone[98]. Here from left to right, cells progressively diminished in size, corresponding to the transition into the meristematic zone. A similar transition was observed in a lateral (xy) image (**Fig. 3.1d**). Another lateral image section of a slightly inclined root revealed root hairs enveloping the root's surface (**Fig. 3.1e**). Imaging the tip of a root, we observed cells that were detached from the primary body of the root near the root cap region (white arrows, **Fig. 3.1f**), reminiscent of border-like cells[99,100] and suggesting that roots grown in the EcoFAB system resemble roots grown in soil. These label-free high-resolution images motivated us to systematically explore the cellular and subcellular features revealed by THG in *B. distachyon* roots, as detailed below.

3.3.2 THG and 3P autofluorescence microscopy imaging of the mature zone of B. distachyon roots

In addition to THG, intrinsic contrast can arise from the autofluorescence of endogenous chromophores in biological specimens. Spectrally separating the THG and 3P autofluorescence signals, we simultaneously acquired THG and 3P autofluorescence images in the mature zone of *B. distachyon* roots (**Fig. 3.2**; Supplementary Video 1 in [101]).

Roots in the mature zone contain concentric layers of epidermis, cortex, endodermis, and vasculature. In epidermis and cortex, THG and 3P autofluorescence signals co-localized at cell walls (**Fig. 3.2a-c**). Even though THG signal was ~3.4–8.8× stronger than 3P autofluorescence signal, cell walls were easily visible in both channels. The contrasting composition of the plant cell wall and the surrounding cytoplasm generated THG signal, while the phenolic compounds in the cell wall[102–104] were likely the source of autofluorescence.

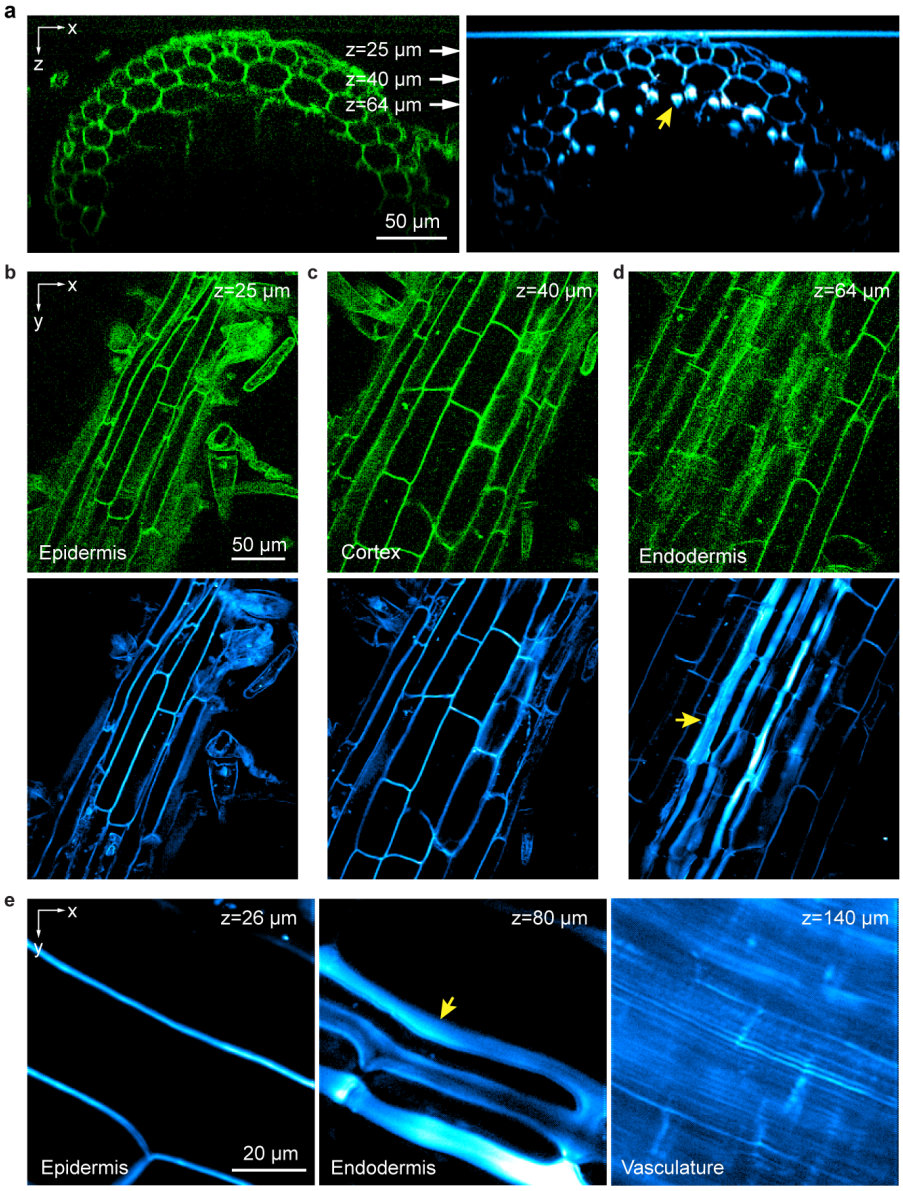

Fig. 3.2 3P autofluorescence and THG microscopy visualize epidermis, cortex, endodermis, and vasculature in the mature root zone of *B. distachyon* roots. (a) 3P autofluorescence (green) and THG (cyan) xz images acquired at 1 µm/pixel showing a cross section of mature root zone. (b-d) xy images acquired at depths indicated by white arrows in a corresponding to putative (b) epidermis, (c) cortex and (d) endodermis tissues. Pixel size: 1 µm/pixel. (e) xy THG images of root tissues at 26 µm, 80 µm, and 140 µm depths, corresponding to putative epidermis, endodermis and vasculature, respectively. Pixel size: 0.3 µm/pixel. Post-objective powers: (a-d) 2.6 mW, (e) 1.2, 1.6, and 14 mW from left to right.

Right before the THG and autofluorescence signals dropped off at larger depths, in the THG images we observed striation features of greater brightness and larger widths than the cell walls above (yellow arrows, **Fig. 3.2a,d,e**). Interestingly, the corresponding autofluorescence image did not exhibit this large increase of brightness (e.g., 65 – 83 μm, Supplementary Video 1 in [101]), suggesting that THG signal was caused by a substantial change in the optical susceptibility. The location and morphology of these bright striated features of ~10 μm width were consistent with Casparian strips in endodermis, which surround the vascular cylinder and regulate the passage of water and other solutes between cortex and vasculature[98]. The distinct molecular composition[105] and thickness of Casparian strips from those of regular cell walls presumably led to its stronger THG contrast. Below the endodermis, vasculature structures were visualized as parallel channels ~1.5 μm apart (**Fig. 3.2e**). Although ~10× higher excitation power was needed for vasculature than for cells in epidermis and Casparian strips in endodermis, we were able to observe structures more than 200 μm deep into the mature root (Supplementary Video 1 in [101]).

3.3.3 THG and 3P autofluorescence microscopy image meristem and root tip of B. distachyon roots at subcellular resolution

Compared with differentiated cells in the mature zone, cells in the meristem region contain more intracellular features required for root growth, which were visualized in the intracellular space in both 3P autofluorescence and THG cross-sectional images of a *B. distachyon* root (**Fig. 3.3a**). As in the mature zone, cell walls generated stronger THG signal than 3P autofluorescence signal and strong THG signal was observed in band-like structures presumed to be Casparian strips (white arrow, **Fig. 3.3a**).

In contrast to cells in the mature zone, cells in the meristem region were less elongated and approximately isodiametric (**Fig. 3.3b-e**). In 3P autofluorescence images, we observed ellipsoidal structures occupying most of the cell volume (**Fig. 3.3b,d**). We speculated that they were enlarged nucleus, a characteristic feature of meristem cells, with their autofluorescence arising from the aromatic chemical structures of nucleic acid molecules themselves[106]. In several nuclei, we found bright and micron-sized autofluorescent aggregates (yellow arrows, **Fig.3. 3b,d**) that were likely nucleoli, whose higher molecular density[107] could lead to the brighter fluorescence observed.

Due to the coherent nature and symmetry requirements of THG, subcellular structures exhibited distinct features in THG images (**Fig. 3.3c,d**) from those of 3P autofluorescence. When the excitation focus was within the optically uniform portion of the cell (e.g., cytoplasm or the non-nucleolus, nucleoplasm part of nucleus)[108], THG signal was minimal. The varying susceptibilities across cytoplasm and nucleoplasm, however, gave rise to strong THG signal at the nuclear envelope (**Fig. 3.3e**). Inside the nuclei, strong THG signal was observed from the putative nucleoli (yellow arrows, **Fig. 3.3c,e**) due to their distinct optical susceptibility from nucleoplasm[108]. In both autofluorescence and THG images, nucleoli were often found near the nuclear envelopes, consistent with previous reports for plant cells[109,110].

The distinctive features of meristem cell nuclei and the strong signal of cell walls in THG images provided us with a label-free method to monitor cell division. For example, we observed a dividing cell with two daughter nuclei close to being separated (dashed box, **Fig. 3.3d,e**). In the equatorial plane[111], a nascent cell wall could be detected in the THG image (red arrow, **Fig. 3.3e**).

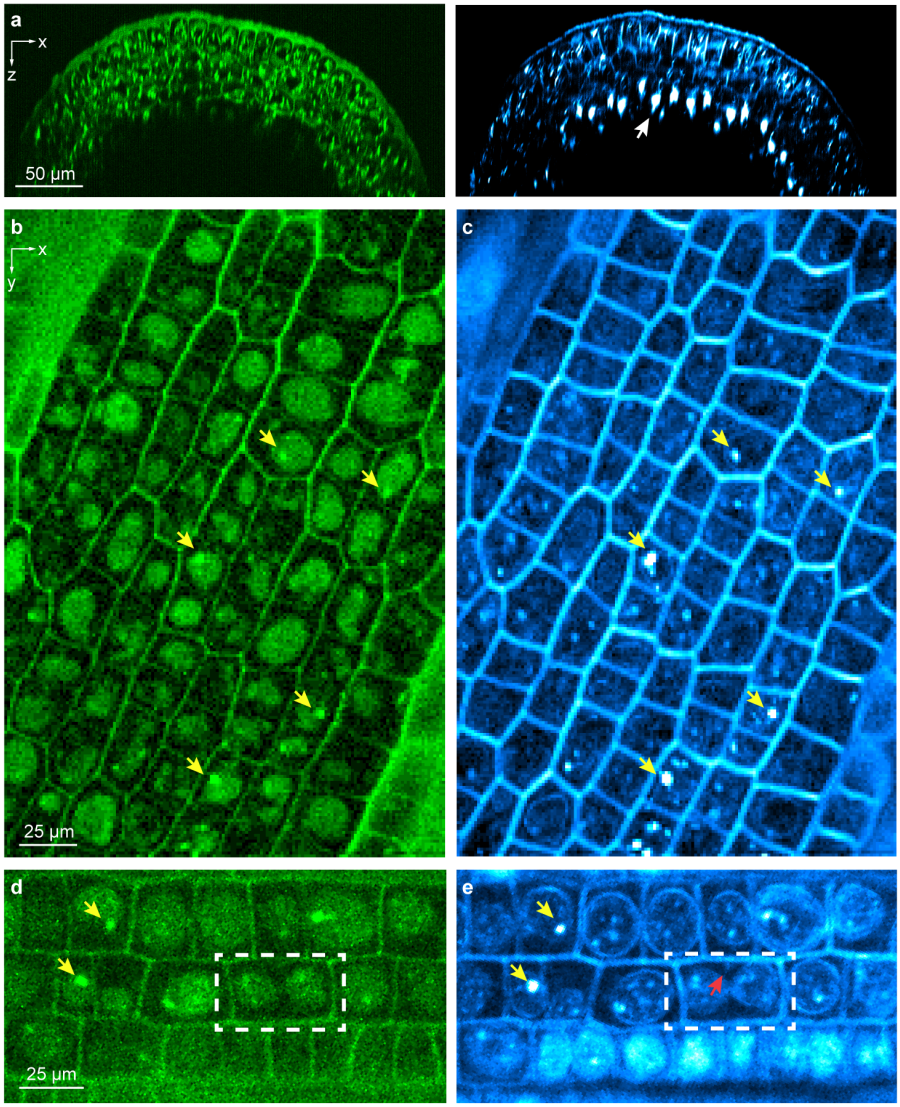

Fig. 3.3 3P autofluorescence and THG microscopy provide label-free imaging of the *B. distachyon* root meristem at subcellular resolution. (a) 3P autofluorescence (green) and THG (cyan) xz images acquired at 0.3 µm/pixel showing a cross section of the root meristem. White arrow: putative Casparian strip. (b-e) 3P autofluorescence (green) and THG (cyan) xy images acquired at (b,c) 0.5 µm/pixel and (d,e) 0.3 µm/pixel. Yellow arrows: putative nucleoli; Dashed white box: a mitotic cell; red arrow: nascent cell wall. Post-objective power: (a) 5.3 mW; (b,c) 5 mW; (d,e) 7 mW.

THG also provided label-free structural contrast at subcellular resolution at the root tip encompassing the apical meristem and the root cap (**Fig. 3.4**). Imaging through a 230-µm-thick root tip (Supplementary Video 2 in [101]), THG revealed a clear boundary between the meristem and the root cap[98] (white arrows in **Fig. 3.4a**, a projected image of a 373 × 310 × 230 µm^3 volume, and **Fig. 3.4b**, a single image section). Putative Casparian strips were found within the THG images of the meristem region but not the root cap region (**Fig. 3.4a**; Supplementary Video 2 in [101]), consistent with known anatomy[98]. An axial cross-sectional view of the apical meristem region showed a complete encirclement of the central vasculature by the Casparian strip (**Fig. 3.4c**). Because light scattering and sample-induced aberration degraded focal intensity at deep depths, the Casparian strips in the bottom half of the root were substantially dimmer than those above. In cells protruding from the tip of the root cap, we observed bright granules of 3-7 µm in size (**Fig. 3.4d**), whose location and morphology were consistent with starch granules[112]. Throughout the apical meristem and root cap, we also saw smaller granules of 1-3 µm in size (**Fig. 3.4e**). We speculated that they may be processing bodies or stress granules[113].

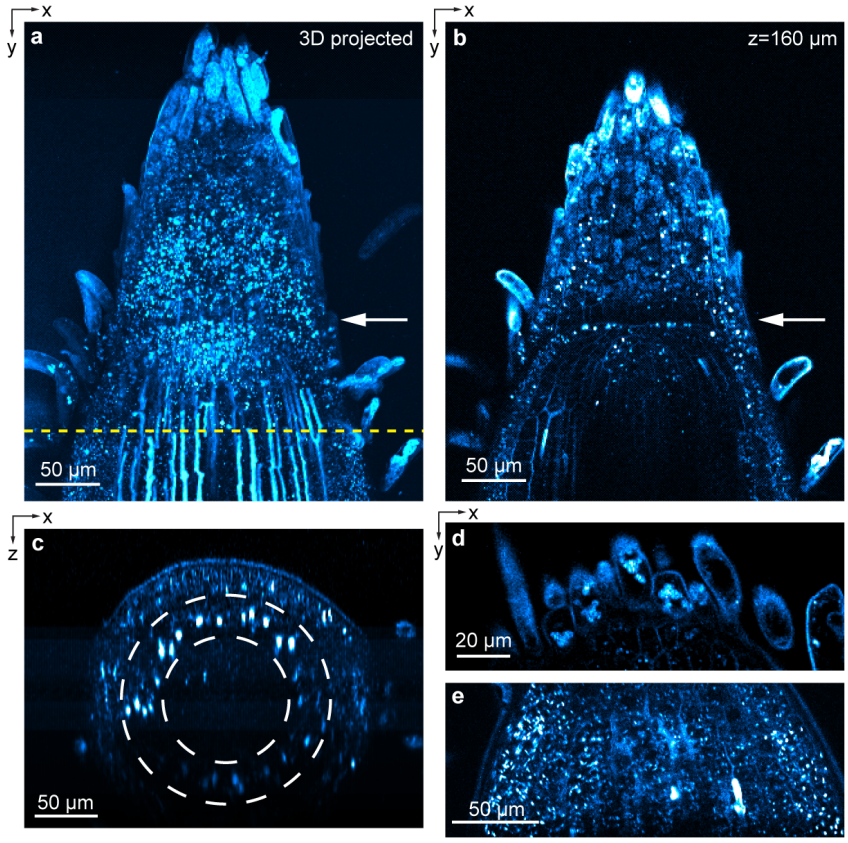

Fig. 3.4 THG imaging of *B. distachyon* apical meristem and root cap. (a) Brightest-spot projection with depth cueing (100% to 50%) of an image stack through a root tip. 230-µm-thick image stack acquired at 1 µm/pixel and z step size of 2 µm. (b) xy image acquired at z=160 µm. White arrows in a,b: boundary between meristem and root cap. (c) xz images acquired along dashed yellow line in a. (d,e) xy images from two other root samples acquired at 0.5 µm/pixel. These roots were placed in between a microscope slide and a coverslip instead of inside EcoFAB to minimize sample motion. Post-objective power: (a-c) 3-15 mW; (d) 4mW; (e) 3.4 mW.

3.3.4 THG and 3PF microscopy enable simultaneous imaging of plant roots and microbes in the rhizosphere

In addition to imaging plant roots themselves, the ability to simultaneously image microbes in the rhizosphere, the region in the vicinity of the roots where the microbiome interacts with the plant, would help understand the complex mechanisms through which root-microbe interactions impact plant growth[114,115]. We found that THG can be combined with 3P to simultaneously image plant roots and bacteria as well as fungi in the rhizosphere *in situ*.

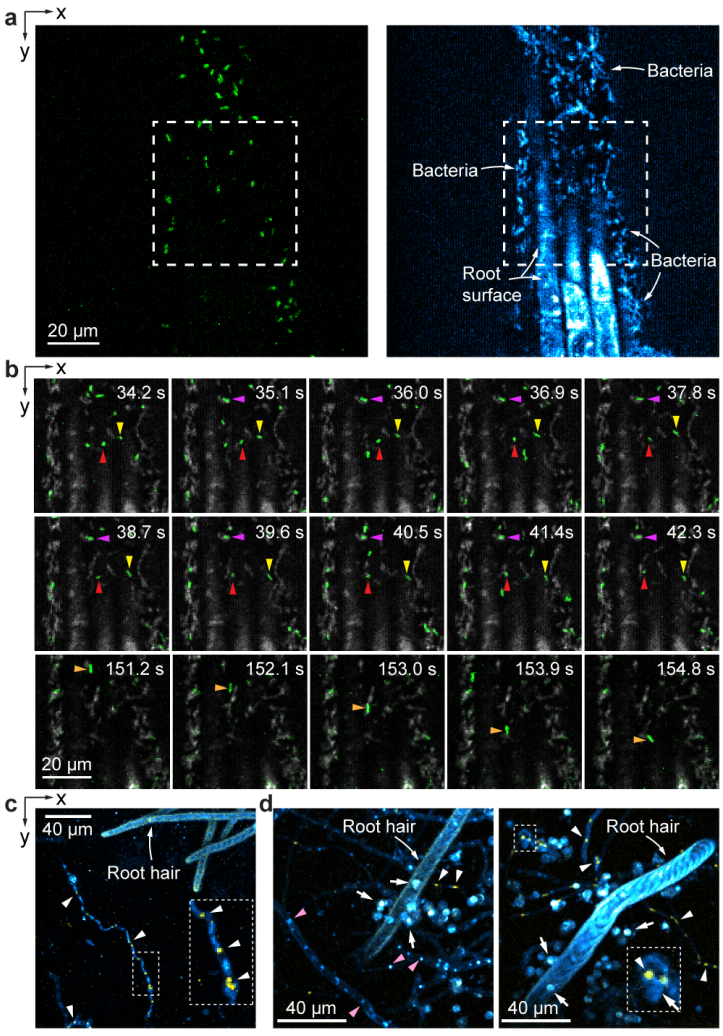

Fig. 3.5 Imaging root-microbe interactions at high spatial and temporal resolution. (a) 3PF (green) and THG (cyan) xy images of *A. thaliana* root inoculated with two strains of *P. simiae* (wildtype *P. simiae* labeled with GFP, mutant *P. simiae* without GFP). (b) Consecutive frames of time-lapse imaging of the dashed box area in a with 3PF in green and THG in gray. Red/purple, yellow, and orange arrowheads: stationary, slowly-moving, fast-moving bacteria, respectively. (c,d) Maximal intensity projected 3PF (yellow) and THG (cyan) images of *B. distachyon* roots inoculated with *T. atroviride* strain IMI with GFP-labeled nuclei. (c) 50-µm-thick image stack acquired at 0.75 µm/pixel and z step size of 2.5 µm. (d) 70-µm-thick image stacks acquired at 0.5 µm/pixel and z step size of 2.5 µm. White arrowheads: GFP-labeled nuclei; pink arrowheads: unlabeled nuclei; white arrows: spores. Insets: zoomed-in views of white dashed boxes. Post-objective power: (a, b) 3.4 mW; (c) 5.6mW; (d) 5.3 mW.

We first imaged two strains of *P. simiae* bacteria[91] near the surface of an *A. thaliana* root, including a GFP-labeled wildtype strain and a mutant strain without fluorescent labeling. Both *P. simiae* strains appeared as rod-like structures in THG images, often forming aggregates around the root tissue (Supplementary Videos 3,4 in [101]; right panel, **Fig. 3.5a**). The GFP-labeled wildtype *P.simiae* had a much stronger 3P fluorescence signal than the autofluorescence from root tissue (left panel, **Fig. 3.5a**) and showed up in both 3PF and THG channels at comparable signal strengths. During the time-lapse imaging over 160 s at 1.1 Hz frame rate (Supplementary Video 4 in [101], **Fig. 3.5b**), we observed stationary (red and purple arrowheads), slowly moving (yellow arrowheads), as well as fast moving (orange arrowheads) bacteria near the *A. thaliana* root. These results indicate that our microscope is capable of simultaneously imaging and tracking of bacteria in the root rhizosphere, and that with additional fluorescence labeling for 3PF, it can image multiple bacterial strains simultaneously.

We also investigated fungal colonization by imaging *B. distachyon* roots inoculated with *Trichoderma atroviride* strain IMI[89,116], which had its nuclei labeled with GFP (H1-GFP[117]). Filamentous structures consistent with fungal hyphae were observed near root hairs in THG images, with their signal likely coming from fungal cell walls (**Fig. 3.5c**). Embedded within these putative hyphal structures were multiple green-fluorescent punctates of 1.5-2.5 μm in size (white arrowheads and inset, **Fig. 3.5c**), in line with the expected sizes of *T. atroviride* nuclei[118]. In another sample, we also found punctate structures in THG images that were not labeled with GFP (pink arrowheads, **Fig. 3.5d**). In addition, spherical features with high THG signal were observed in close proximity to root hairs (white arrows, **Fig. 3.5d**). These spheres were 4-6 μm in diameter and were consistent with being fungal spores, with several of them having colocalized, GFP-labeled nuclei (inset, **Fig. 3.5d**). Therefore, THG microscopy proved to be a valuable tool for visualizing fungal hyphal structures, spores, and nuclei, alongside root structures. When combined with fluorescent labeling, the simultaneous detection of 3PF and THG signals can provide more specific structural insights into the interactions between roots and fungi.

3.4 Adaptive optical third-harmonic generation microscopy for *in vivo* imaging of tissues

3.4.1 AO THG microscope characterization and performance evaluation

We first corrected the optical aberrations of the microscope itself (**Fig. 3.6b-d**). Applying the corrective wavefront for the optical system aberration (**Fig. 3.6d**) led to a ~1.2-fold increase in THG signal of a 150-nm-diameter gold particle (**Fig. 3.6b,c**). The lateral and axial full-widths-at-half-maximum (FWHMs) after AO correction were 0.5 μm and 1.7 μm, respectively, consistent with the diffraction-limited resolution of our system. In all following experiments, the images without aberration correction (labeled "No AO") were acquired after correcting for the aberrations intrinsic to the microscope system.

To validate the ability of our AO module to correct for large wavefront aberrations, we imaged the glass-air interface inside a glass capillary tube (inner/outer diameter: 0.25-0.3 mm/1 mm, 5-000-2005, Drummond). We observed a THG signal improvement of up to 24× and a reduction in the axial FWHM from ~18 μm to 2.8 μm (**Fig. 3.6e,f**), after 4 rounds of aberration correction (correction collar was set to zero; **Fig. 3.6e-h**). Despite the aberration being measured at a single location (asterisk, **Fig. 3.6e**), substantial improvements in image quality were observed across a

field of view of approximately 200 µm. With the central 100 µm, THG signal improvement was larger than 21x (**Fig. 3.6g**). Beyond this range, both the signal enhancement and axial FWHM gradually deteriorated **(Fig. 3.6g)**, due to the spatially variant aberration across the glass capillary tube. The corrective wavefront (**Fig. 3.6h**) indicated large degrees of astigmatism, as expected.

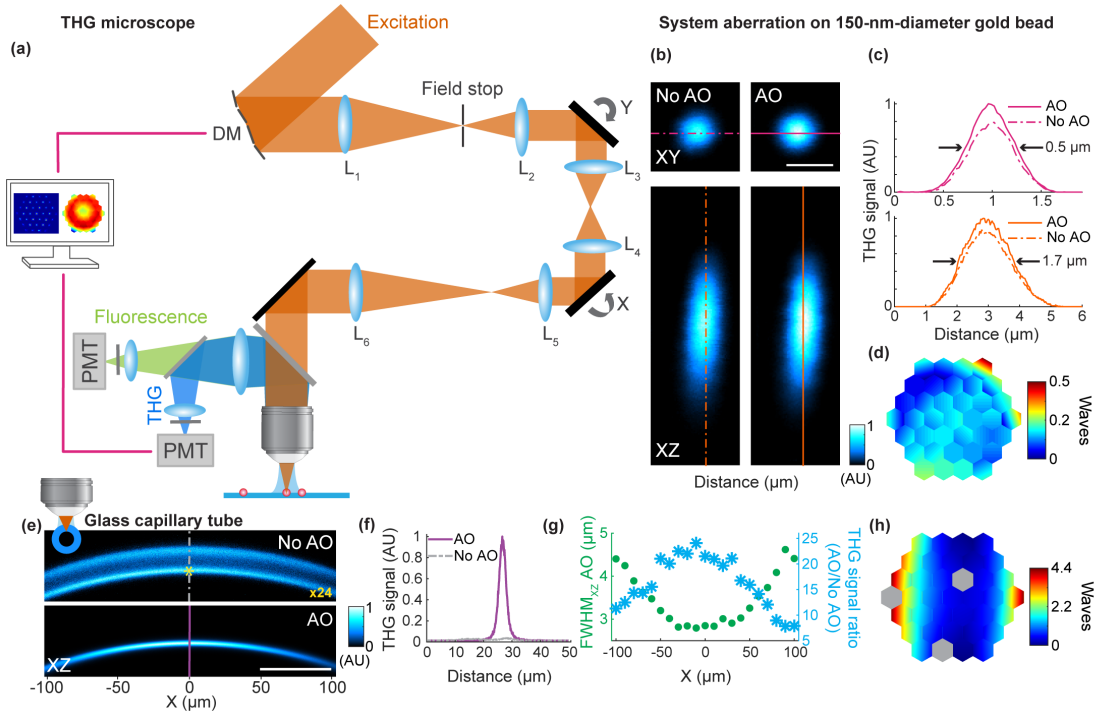

Fig. 3.6 Schematics of the AO THG microscope and system aberration correction, AO improves THG imaging of gold and glass structures under artificial aberrations. (a) Main components of AO THG microscope. DM, deformable mirror; L, lenses; X and Y, galvanometers; PMT, photomultiplier tube. (b) Lateral and axial THG images of a 150-nm-diameter gold bead, under 1,300-nm excitation, before and after system aberration correction. (c) Signal profiles along pink and orange lines in (b). (d) Corrective wavefront. (e) Axial THG images of the glass-air interface inside a capillary tube (objective correction collar set to zero), without AO correction and after running the aberration measurement a total of 4 iterations. 24-fold digital gain was applied to No AO image to increase visibility. Yellow asterisk indicates the location of aberration measurement. (f) Signal profiles along the purple and gray lines in (n). (g) Axial FWHM of line profiles taken on AO image in (n) (green circles) and THG signal improvement (AO/No AO, blue asterisks) as a function of the position X. (h) Corrective wavefront in (e). Grayed-out regions indicate broken mirror segments at the time of experiment. Post-objective power: 1 mW in (b), 3 mW in (e). Scale bars, 1 µm in (b), 50 µm in (e).

3.4.2 In vivo plant root imaging

We also tested how well our AO module improved the image quality of label-free THG microscopy in highly scattering root tissues. Here, we used *B. distachyon*[83,119], a monocot grass that has emerged as an important model system due to its genetic tractability and close relationship with grass crops. Compared to *A. thaliana*, another well-known model plant with semitransparent roots[85], the roots of *B. distachyon* are more optically opaque, thus benefit from the long excitation wavelength of THG.

We performed *in vivo* AO THG imaging of *B. distachyon* roots through a glass coverslip that formed the root chamber of the EcoFAB devices (**Fig. 3.7a**). The correction collar of the microscope objective was set to zero. Imaging was performed in the mature zone of the root, where elongated cells possessed strong THG signals at their cell walls. AO improved cell-wall THG signal by ~2-2.5× (**Fig. 3.7b-f**). In lateral images (**Fig. 3.7c**, zoomed-in views of the area within the dashed box in **Fig. 3.7b**), a few micron-sized gaps between neighboring cell walls were only resolvable after aberration correction (**Fig. 3.7d**). After applying corrective wavefront (**Fig. 3.7g**), we also observed ~2× increase in cell wall signal in both the epidermis layer and the cortex layer of the root in axial images, enabling better visualization of cells in deep layers (**Fig. 3.7e,f**). Given the shallow depth of the root tissue imaged, aberration correction likely mostly compensated for the aberration introduced by the coverslip.

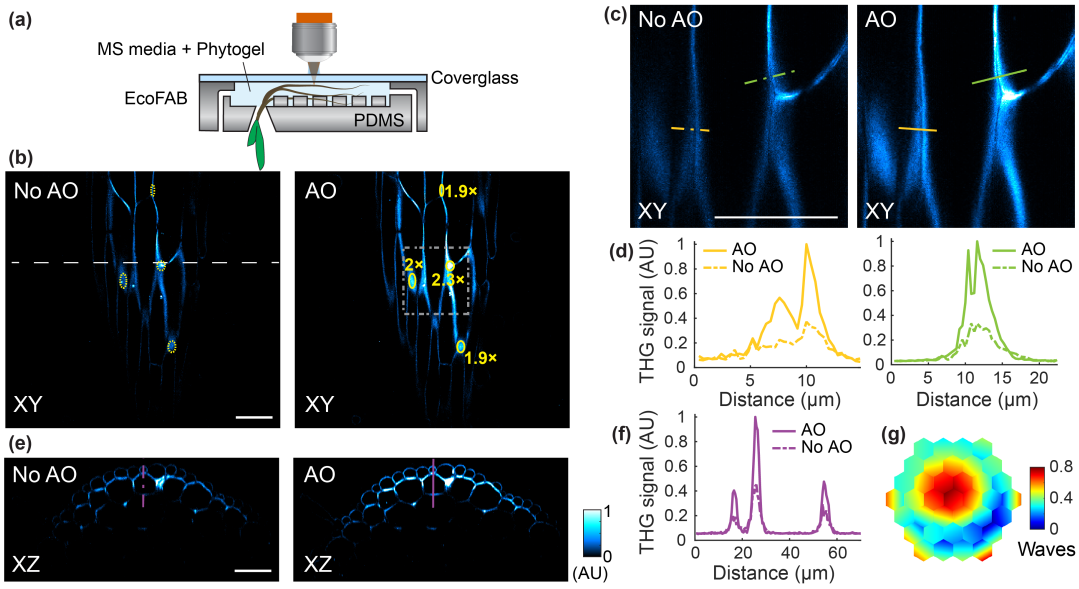

Fig. 3.7 AO improves THG *in vivo* imaging of *B. distachyon* root tissues. (a) Schematic showing the EcoFAB growth chamber used for imaging the roots of *B. distachyon*. Note that the EcoFAB is inverted for imaging. (b) Lateral THG images of the mature zone of a *B. distachyon* root, under 1,300 nm excitation, without and with AO. Ratio of the averaged THG signals within the yellow ovals in (a,b,e,h,i) is indicated. Post-objective power: 2.2 mW. (c) Zoomed-in views of the area in the dashed box in (b). (d) Signal profiles along the orange and green lines in (c). (e) Axial THG images along the dashed line in (b) acquired without and with AO. Post-objective power: 2.7 mW. (f) Signal profiles along the purple lines in (e). (g) Corrective wavefront. Scale bars, 50 μm.

3.5 Conclusion and discussion

3.5.1 THG microscopy provides great potential for root biology

THG microscopy combined with microfabricated ecosystems allowed us to capture subcellular-resolution images of living plant roots without extrinsic fluorescent labels. Because THG signal originates from heterogeneity of optical susceptibilities within the excitation focal volume, it generates label-free visualization of cell walls. The 1.3-μm excitation light penetrated deep into the opaque tissues of *B. distachyon* roots, which are ~2.5× thicker[120] than the more widely studied

and optically transparent roots of *A. thaliana*, and enabled us to visualize the vasculature in mature roots and image through the entirety of a 230-μm-thick root tip. Given that all cells in plant roots possess cell walls generating strong THG signal, THG microscopy can provide organ-scale views of root structures at subcellular resolution. In contrast to electron microscopy, which also offer a view of subcellular features, THG microscopy can be applied to live roots without labeling. Furthermore, due to its distinct wavelength, THG signal can be combined with simultaneously acquired fluorescent signals, either from the autofluorescence of endogenous molecules or from exogenous fluorescent labels, to provide structural context for biological processes of interest.

The structural features we observed in THG images are consistent with the known anatomy of plant roots. These include root hairs and elongated cells in the mature root zone. In both mature and meristem roots, we observed the layered arrangement of epidermis, cortex, and endodermis. Within endodermis, we found longitudinal striation features with strong THG signal that terminated at the root cap and were consistent with the location and morphology of Casparian strips. In the root meristem, THG contrast allowed us to visualize nucleoli and nuclear envelopes, providing information on stages of cell division. These structural identifications were strengthened by simultaneously recorded 3P autofluorescence signals from cell walls, nuclei, and nucleoli. In both apical meristem and root cap, between which a clear boundary can be identified in their THG images, the subcellular resolution of our imaging system allowed us to visualize and differentiate granules of varying sizes. Whereas starch granules were observed in root cap cells and border-like cells, we speculated that the small and bright punctates throughout meristem and root cap were likely stress-related granules, whose identities need to be further confirmed with molecular labeling approaches.

In addition to providing global structural information throughout the plant roots at subcellular resolution, THG microscopy also allows one to image bacteria and fungi in the rhizosphere. Because both bacteria and fungi have cell walls, they could also be visualized in a label-free manner by THG microscopy. Transgenic bacteria and fungi with fluorescent protein labels further improve the specificity of structural imaging. With multimodal THG and 3FP imaging, we were able to observe dynamics of bacterial distribution and fungal spores and hyphae near roots *in situ*. With deep penetration depth and optical sectioning capability, THG and 3PF microscopy therefore enable the investigation of root-microbe interactions throughout the rhizosphere and within plant roots at high spatial and temporal resolution.

It should be noted, however, that plant cells are susceptible to light- and/or heat-induced damages, especially during multiphoton excitation[121,122]. In our experiment, extended imaging of meristem zone at post-objective powers over 10 mW always induced damage in the form of increasing the amount of bright punctates. Mature zone, on the other hand, withstood prolonged imaging at tens of mW without exhibiting visible damage. Care should always be taken to ensure that the biological process of interest is not unduly perturbed by imaging.

Our combined EcoFAB and multimodal imaging approach provides a powerful tool for studying the cellular structure of the roots. The large imaging depth of THG and 3PF microscopy enables the study of root-penetrating bacteria in opaque root tissues[123]. THG microscopy's ability to visualize dividing root cells will enable studies on cellular division, elongation, and differentiation during root growth. Growth conditions could be altered within the EcoFAB chamber – providing a testbed for investigating how roots respond to environmental conditions, such as salinity or nutrient levels[124], at high spatiotemporal resolution. In summary, by integrating microfabricated systems with nonlinear optical microscopy for label-free imaging of plant roots, we expect that

our approach will illuminate the "hidden half" of the plant, shedding light on numerous unexplored facets of root biology.

3.5.2 AO THG microscopy extends the application of both AO and THG

In this work, we combined a compact AO module with a THG microscope and achieved high-resolution label-free imaging of a variety of biological and non-biological samples. Taking advantage of the exceptional ability of THG microscopy to generate contrast from heterogeneities in specimen optical properties, along with the NIR excitation wavelengths used here (i.e., 1,300 nm), our AO THG microscope allowed us to clearly visualize key anatomical features in highly scattering biological tissues of *B. distachyon* roots *in vivo*, without the need for exogenous labelling agents. The image quality improvement achieved after aberration correction was observed consistently across the imaging field of view of up to hundreds of microns in dimension, consistent with previous studies using fluorescence microscopy[8,47,51,53].

Using bright THG-producing non-biological samples, including glass interfaces, our AO module enabled the correction of large amounts of aberration, leading to substantial improvements in the THG signal along with a reduction in the axial extent of the intensity PSF down to the diffraction-limit.

Using our AO THG microscope, we performed label-free subcellular-resolution *in vivo* imaging within the highly scattering root tissues of *B. distachyon*. Here, aberration correction led to improvements in image quality, greatly improving the visibility of root structures including cell walls. While previous studies have shown that the THG signal from dielectric materials[125] and various biological tissues[24–26] can be used for aberration correction, to the best of our knowledge, our results constitute the first demonstration of aberration correction using the endogenous THG signal generated within the previously mentioned highly-scattering biological systems. The combination of AO with label-free THG imaging as shown here opens the door for studying biological phenomena in vivo in model systems lacking fluorescence labeling such as plants.

In scenarios where the THG signal significantly outweighs any endogenous or exogenous fluorescence signals, conducting the aberration measurement procedure utilizing the THG signal offers advantages. This approach allows for the utilization of lower excitation powers during aberration measurement, a particularly important consideration in highly photosensitive samples such as plant root tissues.

Besides the ability to correct for the optical aberrations introduced by tissues, our AO module effectively compensated for other sources of aberration intrinsic to the experimental setup. In this work, this included the spherical aberration introduced by the glass windows used to gain optical access to tissues, such as the EcoFAB root chamber. Correcting for these sources of spherical aberration becomes especially important when the microscope objective lacks a correction collar. When a correction collar is available, AO can still correct for the additional aberration modes, such as coma and astigmatism, that originate from a tilted window[126]. Lastly, our AO module would be highly beneficial for sample preparations (surgical or otherwise) that introduce substantial aberrations, such as those requiring thick/tilted glass windows or microprisms.

Chapter 4

Third-Harmonic Generation Microscopy with Homodyne Detection

4.1 Introduction

In **Chapter 3**, we have pointed out that the harmonic generation signal originates from a material's nonlinear susceptibility and offers potential for label-free imaging. We later demonstrated THG microscopy's capability to probe general structural information in plant root samples. Here, we emphasize that a material's nonlinear susceptibility depends not only on its intrinsic properties but is also inversely related to the difference between the material's resonant frequency and the excitation light's fundamental frequency or its harmonics[127]. Notably, harmonic generation imaging typically operates far off the material's resonances, a condition that is especially common in bioimaging applications, often resulting in low nonlinear susceptibility and significantly reduced optical conversion efficiency for the harmonic generation process[27]. As a result, the generated signal is relatively weak, and the signal-to-noise ratio (SNR), scaling with $\sqrt{N}$ (where N is the number of detected photons), is limited. While increasing the incident laser power can improve conversion efficiency, it also introduces the risk of photo- or heat-damage to the sample. In **Chapter 3**, we discussed how high-power illumination caused damage to plant roots, limiting our ability to perform continuous imaging or long-term studies.

Thus, finding an alternative approach to enhance weak signals during the imaging of biological samples remains crucial, as these samples are primarily composed of weakly nonlinear components. Enhancements have been demonstrated through adjusting the excitation wavelength, either by exploiting the resonant enhancement of the target biological component[29,128] or by optimizing phase-matching conditions through dispersion[30]. However, these wavelength-tuning approaches need to be tailored to the optical properties of specific structures of interest, making them less effective for imaging diverse or unknown biological samples.

4.2 Optical homodyne detection

Optical homodyne detection, an alternative approach for enhancing the measurement of weak optical radiation, was introduced shortly after the invention of the laser[31,129]. Broadly defined, homodyne detection enhances signal extraction by comparing the signal with a reference oscillation of the same frequency. Specifically for harmonic generation imaging, this technique leverages the coherent properties of SHG or THG signals.

For n-th order harmonic generation from the fundamental light at frequency ω, the homodyne detection approach amplifies the sample harmonic signal at $\omega_{\mathrm{n}} = n\omega$ by pre-generating a reference light at the same frequency ω_{n} from the same fundamental light to coherently interfere with it[28,130].

Homodyne detection has been demonstrated with the interference occurring either at the detector[131,132] or within the sample itself (including at the surface of interest)[28,133]. When interference occurs within the sample, it is sometimes referred to as "optical stimulation", reflecting the physical process of wave mixing in the nonlinear medium. While the two scenarios exhibit practical differences in their implementation, they are considered equivalent descriptions of the same physical interaction under quantum electrodynamical treatment[134,135]. In either scenario, at the position where the reference field $\tilde{E}_{\mathrm{r}}$ and the sample harmonic signal field $\tilde{E}_{\mathrm{s}}$ interfere, the light field oscillating at harmonic frequency ω_{n} can be written as:

$$\tilde{E} = E_{\mathrm{r}} e^{-i(\omega_{\mathrm{n}} t - \varphi_{\mathrm{r}})} + E_{\mathrm{s}} e^{-i(\omega_{\mathrm{n}} t - \varphi_{\mathrm{s}})}, \tag{4.1}$$

in which φ_{r} and φ_{s} are the phase offsets of two fields, respectively. Therefore, the intensity measured by the detector at the harmonic signal wavelength depends on the relative phase between the two light fields $\Delta\varphi = \varphi_{\mathrm{s}} - \varphi_{\mathrm{r}}$, and can be expressed as:

$$\begin{aligned} I_{\mathrm{det}}(\Delta\varphi) &= I_{\mathrm{r}} + I_{\mathrm{s}} + 2\sqrt{I_{\mathrm{r}} I_{\mathrm{s}}} \cdot \cos(\Delta\varphi), \\ &= I_r + I_s + I_{\mathrm{HD}}(\Delta\varphi) \end{aligned} \tag{4.2}$$

where I_{r} is the intensity of the reference light, I_{s} is the intensity of the sample harmonic signal. Here, $I_{\mathrm{HD}}(\Delta\varphi)$ is the signal induced by the homodyne process:

$$I_{\mathrm{HD}}(\Delta\varphi) = I_{\mathrm{HD}}^{\mathrm{max}} \cdot \cos(\Delta\varphi) = 2\sqrt{I_{\mathrm{r}} I_{\mathrm{s}}} \cdot \cos(\Delta\varphi) \tag{4.3}$$

with

$$I_{\mathrm{HD}}^{\mathrm{max}} = 2\sqrt{I_{\mathrm{r}} I_{\mathrm{s}}} = 2\sqrt{\kappa}\sqrt{I_{\mathrm{r}} I_{\mathrm{f}}^{\mathrm{n}}}, \tag{4.4}$$

in which the nonlinear relation for the n-th order harmonic generation process, $I_{\mathrm{s}} = \kappa I_{\mathrm{f}}^{\mathrm{n}}$, is taken into account with a proportional factor κ representing the efficiency of the harmonic generation process and the fundamental light intensity being I_{f}. By adjusting relative phase $\Delta\varphi$, I_{HD} can be increased and made positive, and thereby enhancing the signal measurement I_{det} until I_{HD} reaches its maximum value $I_{\mathrm{HD}}^{\mathrm{max}}$. The maximum homodyne enhancement is then given by the factor:

$$\eta = \frac{I_{\mathrm{HD}}^{\mathrm{max}}}{I_{\mathrm{s}}} = 2\sqrt{\frac{I_{\mathrm{r}}}{I_{\mathrm{s}}}}. \tag{4.4}$$

This equation indicates that a stronger reference light compared to a given spontaneous harmonic signal leads to a greater enhancement factor. In past research, enhancement factors η greater than

10^4 for SHG imaging of collagen[133] and greater than 3000 for THG imaging of calcium fluoride slide[28] have been reported, suggesting a great promise of the homodyne enhancement.

In addition to signal enhancement and improved SNR, homodyne detection offers the potential to probe the phase information of a sample's harmonic generation signal through multiple measurements with shifted relative phases $\Delta\varphi$. This capability was first demonstrated in 1965 by Chang et al. to determine the complex nonlinear susceptibility of various semiconductor materials[136]. The technique remained primarily within material science applications[130–132,137,138] until the 2010s, when it was extended to SHG imaging of biological samples to reveal the relative orientation of noncentrosymmetric structures such as myosin filaments, tendons, and mitotic spindles[139–141].

4.3 Acquiring homodyne-enhanced images with harmonic generation microscopy

From eqn. 4.4, even achieving an η just greater than 10 already requires I_r to be about two orders of magnitude higher than I_s. However, the I_r term in eqn. 4.2 exists independently of the harmonic generation process and does not carry sample information, but it can overwhelm the actual signal in the measurement. To acquire a homodyne-enhanced sample image I_0, I_r should be treated as a background term in eqn. 4.2 that requires elimination. Meanwhile, the sample information is encoded in I_s and I_{HD}, with I_{HD} being the enhanced signal term central to this method. Maximizing I_{HD} to $I_\mathrm{HD}^\mathrm{max}$ and extracting a readout either proportional to $I_\mathrm{s} + I_\mathrm{HD}^\mathrm{max}$ or $I_\mathrm{HD}^\mathrm{max}$ would achieve the goal of acquiring a homodyne-enhanced sample image.

In principle, there are two straightforward approaches that involve taking only two images. One approach is to take an image with both the fundamental and the reference light coincident on the sample, yielding a detected signal $I_1 = I_\mathrm{s} + I_\mathrm{r} + I_\mathrm{HD}^\mathrm{max}$ at each pixel after careful adjustment of the relative phase $\Delta\varphi$, and another image with the fundamental light blocked, recording only $I_2 = I_\mathrm{r}$. Subtracting I_2 from I_1 provides enhanced sample image $I_0 = I_\mathrm{s} + I_\mathrm{HD}^\mathrm{max}$. As another option, subtracting two images taken with a π phase shift in φ_r can result in $I_0 \propto I_\mathrm{HD}^\mathrm{max}$, which also provides sample information[139].

Building on this approach, performing multiple measurements with phase shifts in $\Delta\varphi$ allows the relative phase information of the harmonic generation signal φ_s to be determined in addition to the enhanced sample signal[139,140]. For example, Bancelin et al. used 9 images with reference phase varying at $\pi/3$ phase steps to extract both the amplitude and relative phase of a mitotic spindle image[141].

The above approaches, involving taking several separate images, may face challenges related to low-frequency noise originating from sample motion, fluctuating laser output, and environmental influences like air currents and optical table instabilities[142]. Alternatively, applying high-frequency modulation to the reference or the fundamental field, followed by demodulation of the detected signal, can be used to extract I_sample at each pixel. Goodman et al.[133] and Stock et al.[28] demonstrated amplitude modulation of the fundamental light at each pixel using a mechanical optical chopper at 3 kHz in SHG imaging and 30 kHz in THG imaging, respectively, so that I_det oscillated at the corresponding frequency. The pixel value can then be acquired through a lock-in amplifier that reads out the amplitude of oscillation, yielding output $I_0 \propto I_\mathrm{s} + I_\mathrm{HD}^\mathrm{max}$ after optimizating the relative phase. Alternatively, Yazdanfar et al.[132] presented a method with phase

modulation at 100 Hz using a piezo-mounted mirror oscillating longitudinally in the reference arm, followed by phase-sensitive demodulation of the detected signal. Gao et al.[142] further advanced the method by using an electro-optic modulator (EOM) for fast phase modulation of either light field up to 1 MHz, followed by phase-sensitive lock-in amplification. The advantage of using phase modulation over amplitude modulation is that the amplitude readout at each pixel for phase modulation already ensures a maximized $I_{\mathrm{HD}}^{\max}$, while simultaneously acquiring the relative phase information φ_{s}. Notably, although the aforementioned methods can filter out low-frequency noise, the frequency-independent photon noise associated with I_{r} still exists and can potentially overwhelm the real signal, requiring a balance between photon noise and signal enhancement through power allocation to the fundamental and reference light.

Among harmonic generation imaging modalities, THG microscopy is applicable to a broader range of samples and structures, making it particularly useful for probing diverse structures in general biological samples. As it often suffers from low signal, this challenge motivated us to develop and demonstrate THG microscopy with homodyne detection for imaging biological samples, specifically plant roots—a technique that, to our knowledge, has yet been demonstrated on biological imaging.

4.4 System setup

The experimental setup is depicted in **Fig. 4.1**. The excitation source consists of an optical parametric amplifier (Opera-F, Coherent), which is pumped by a 40-W femtosecond laser (Monaco 1035-40-40, Coherent). Opera-F is tuned to generate 1,600 nm output at a 1 MHz repetition rate, with an average output power of 0.75 W and a pulse width of ~50 fs. This excitation power is split into two arms for the fundamental and reference lights using a motorized half-wave plate (M-HWP, DDR25 and WPH10E-1625, Thorlabs) and a polarized beam splitter (PBS, CCM5-PBS204, Thorlabs), which control the relative power between them.

In the reference arm, the polarization of the excitation light is first rotated by a half-wave plate (HWP, AHWP05M-1600, Thorlabs) to match the polarization in the fundamental arm. The 1600 nm excitation light is then frequency-tripled through two beta barium borate (BBO) crystals C1 and C2. First, it passes through C1 (0.5 mm thickness, P-coating, BTC5050-SHG1600(I)-P, Newlight Photonics) for Type I SHG, generating 800 nm light. Next, both the 800 nm and 1600 nm beams pass through C2 (0.25 mm thickness, P-coating, BTC5025-THG1600(II)-P, Newlight Photonics) for Type II sum-frequency generation (SFG), producing 533 nm reference light. Two crystals are positioned close together near the focus between a pair of lenses (L1 and L2, f = 100 mm, AC254-100-C-ML and LA1509-A-ML, Thorlabs) to achieve higher efficiency for frequency tripling. Residual 1600 nm and 800 nm radiation after C1 and C2 is filtered out using a colored glass bandpass filter (GBP, FGS600M, Thorlabs) and a Glan laser polarizer (GLP, GL10-A, Thorlabs), followed by a beam dump (BD, LB1, Thorlabs).

In the fundamental arm, the fundamental light is phase-modulated with an electro-optic modulator (EOM, M-360-40-02 LTA Dry, Conoptics) at up to 1 MHz. For simpler implementation when phase measurement is not needed, the EOM can be replaced by an optical chopper (CHP, MC1F10HP, Thorlabs) for amplitude modulation up to 1 kHz. The fundamental light is directed to a delay stage (DS) consisting of two mirrors mounted on a linear translation stage (Model 436 and SM-50, Newport).

The reference and fundamental lights recombine after passing through a dichroic mirror (Di, FF835-SDI01-T1, Semrock) and are scanned by two conjugated galvanometric scanning mirrors (X and Y, 6215H, Cambridge Technology). The light is relayed to the back-pupil plane of a high NA water-dipping objective (Olympus XLPLN25XWMP2, NA 1.05, 25×) by two pairs of scan lenses (SL50-2P2 and SL50-2P2, SL50-2P2 and TTL200MP; Thorlabs), and through a 50:50 beam splitter (50:50 BS, BSW29R, Thorlabs). The objective is mounted on a piezoelectric stage (P-725.4CD PIFOC, Physik Instrumente) for axial translation of the excitation focus. The THG signal is collected by the same objective, reflected by the 50:50 BS, and detected by a photomultiplier tube (H10770PA-40, Hamamatsu) through an emission filter (FF03-525/50-25, Semrock).

4.5 Practical considerations

There are two criteria for achieving homodyne detection with the system shown in **Fig. 4.1**.

First, the reference light and the fundamental light must propagate collinearly when entering the objective. To achieve this at any arbitrary scanning angle within the field of view, the spatial overlap of the two beams must be maintained from before they enter the scanning mirrors to their arrival at the back pupil of the objective. This overlap can be verified using a camera.

Second, temporal overlap is also critical. Since the excitation source has a very short pulse width (~50 fs), the two light beams must arrive at the sample plane within this duration for interference to occur. This requires the optical path length difference between the two arms to be less than 15 μm, which can be adjusted using the delay stage. Once spatial overlap is confirmed, temporal overlap can be tested using a separate BBO crystal (not shown in **Fig. 4.1,** 1 mm thickness, P-

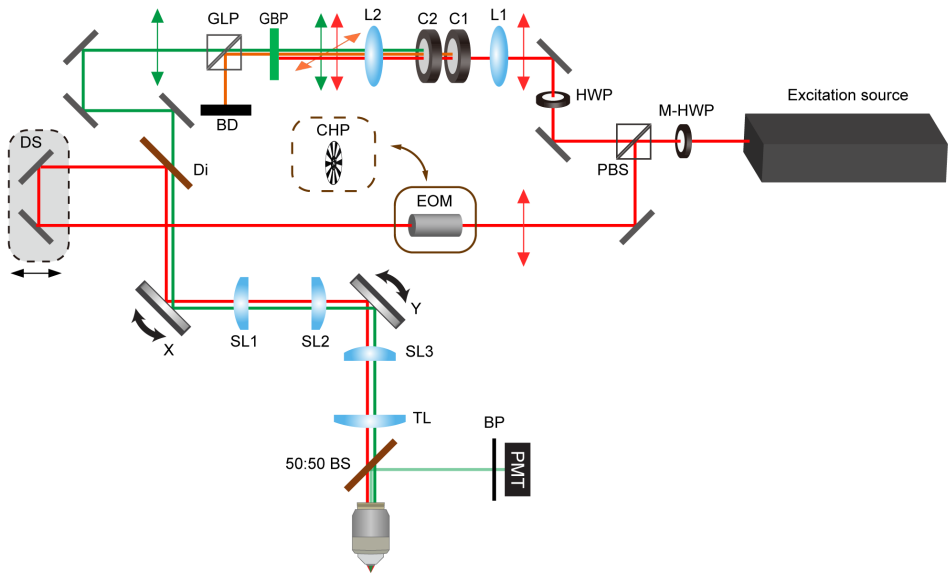

Fig. 4.1 Optical setup for the third harmonic generation microscopy with homodyne detection. M-HWP: motorized half-wave plate; PBS: polarized beam splitter; HWP: half-wave plate; L1 and L2: focusing lenses; C1 and C2: BBO crystals; GBP: colored glass bandpass filter; GLP: Glan laser polarizer; BD: beam dump; EOM: electro-optic modulator; CHP: optical chopper; DS: delay stage; Di: dichroic mirror; X and Y: galvanometric scanning mirrors; SL1, SL2 and SL3: scan lenses; TL: tube lens; 50:50 BS: 50:50 beam splitter; BP: bandpass filter; PMT: photo multiplier tube.

coating, BTC5100-4HG1600(I)-P, Newlight Photonics) designed to generate 400 nm light through SFG from the 1600 nm fundamental and 533 nm reference beams. If 400 nm light is detected with the camera after the crystal through a narrow bandpass filter (FBH400-40, Thorlabs), it confirms that both spatial and temporal overlap have been achieved. Additionally, if the optical chopper is used instead of the EOM, an extra phase plate, such as a glass plate with adjustable tilt, can be introduced into either arm for fine-tuning the relative phase $\Delta\varphi$ between the two light beams to achieve the maximum homodyne signal.

Practically, both overlap criteria should be checked starting from their merger at Di. They must also be verified sequentially after each accessible optical component, as collinearity and temporal overlap will change due to dispersion when propagating through the optical components.

4.6 Current stage and future plans for the project

The optical setup shown in **Fig. 4.1**, including the two light path arms and the delay stage, has been assembled and aligned. An initial power allocation, serving as a starting point, directed 600 mW of the 800 mW laser output to the fundamental arm to produce an I_s just above the PMT's detection limit, with the remaining laser power directed to the reference arm. By optimizing the frequency tripling section of the reference arm, we achieved a maximum output of 18.8 mW from a 204 mW input, corresponding to a conversion efficiency of 9%. However, the transmittance of the reference light from its generation to the back pupil of the objective is too low, resulting in no detectable signal (<5 nW) under the objective. Further optimization of the optical components in the path is necessary. Power allocation will also require iterative adjustments to optimize the system.

Meanwhile, the spatial and temporal overlap of the two light beams is expected to be aligned in the near future. Once these challenges are resolved, a test run of the homodyne imaging should be conducted using an artificial sample, such as a glass slide, to record both the background reference signal and the spontaneous THG signal, and to demonstrate the homodyne-enhanced THG. The final step will be to image the plant root using the microscope.

Chapter 5

Conclusion

This thesis has explored and advanced several aspects of optical microscopy, particularly in the context of high-resolution optical sectioning imaging techniques for live biological systems. Focusing on challenges such as optical aberrations, label-free imaging, depth penetration, and signal strength, this work has contributed to the fields of both linear and nonlinear optical microscopy, including imaging modalities such as confocal microscopy, 3PF microscopy, and THG microscopy.

In **Chapter 2**, we addressed optical aberrations in confocal fluorescence microscopy. Through the introduction of AO, we were able to measure and correct common wavefront aberrations in biological samples. This chapter particularly focused on a novel AO method based on frequency-multiplexed aberration measurement, which was integrated into confocal microscopy. The results demonstrated the ability of this method to improve imaging performance using intrinsic fluorescence features of any size, effectively correcting large-magnitude aberrations and enhancing image quality and resolution in challenging biological systems, such as zebrafish larvae and live mouse brain.

In **Chapter 3**, we explored the application of 3PF and THG microscopy for imaging live plant roots *in situ*. These techniques provided significant improvements in imaging depth in opaque *B. distachyon* roots compared to conventional single-photon methods, enabling us to visualize the entire root tip and down to the vasculature layer of the mature root zone. We successfully imaged various root structures, demonstrating the potential for subcellular resolution imaging without fluorescence labeling. Simultaneously recorded 3PF signals also allowed us to investigate root-microbe interactions at high spatiotemporal resolution. We then applied our frequency-multiplexed AO method to correct optical aberrations in THG microscopy. Using THG signals from the glass-air interface and root cell walls, we demonstrated that our AO method effectively corrects large aberrations in the former and corrects aberrations in live, label-free plant samples from the latter, significantly enhancing the utility of THG for biological imaging and broadening the application of our AO method.

In **Chapter 4**, the focus shifted to improving the sensitivity of THG microscopy. This chapter addressed the challenge of weak conversion efficiency in the THG process within biological

samples, a limitation previously discussed in **Chapter 3**, and reviewed existing methods to overcome this issue. Among these methods, homodyne detection was identified as an effective approach with minimal side effects for the biological imaging application of our interest. This technique leverages the coherence of the THG signal by pre-generating a reference light with identical wavelength to the sample harmonic signal, which interferes with and amplifies the latter. An overview of the optical homodyne field was provided, along with a THG microscopy system incorporating homodyne detection that I designed. Currently, the optical setup has been assembled, but further alignment to ensure spatial and temporal overlap between the two light paths, as well as optimization of the optical components to improve transmittance, is needed.

In conclusion, the research presented in this thesis has advanced state-of-the-art in both linear and nonlinear optical microscopy techniques. By addressing key challenges such as optical aberrations, depth penetration, label-free imaging, and signal enhancement, this thesis contributes to the development of more robust and versatile microscopy methods for biological research. The integration of frequency-multiplexed AO with confocal microscopy, the application of THG for label-free deep tissue imaging in plant roots, and the introduction of homodyne THG microscopy for enhancing low signal bioimaging represent significant advancements in achieving high-resolution optical-sectioned imaging of living biological systems.

Future work will focus on the further optimization of the homodyne THG system to enable its application in THG imaging of both artificial and natural samples. This will facilitate long-term *in situ* studies of plant roots and other living biological systems. Additionally, the methodologies and findings outlined in this thesis lay the foundation for the development of new high-resolution, non-invasive imaging tools, offering significant potential for a wide range of biological applications.

References

1. Mertz, J. *Introduction to Optical Microscopy*. (Cambridge University Press, 2019).
2. Conchello, J. A. & Lichtman, J. W. Optical sectioning microscopy. *Nature Methods 2005 2:12* **2**, 920–931 (2005).
3. Pawley, J. B. *Handbook of Biological Confocal Microscopy*. *Handbook of Biological Confocal Microscopy: Third Edition* (Springer, 2006). doi:10.1007/978-0-387-45524-2.
4. Denk, W. *et al.* Anatomical and functional imaging of neurons using 2-photon laser scanning microscopy. *J Neurosci Methods* **54**, 151–162 (1994).
5. Wan, P. *et al.* Evaluation of seven optical clearing methods in mouse brain. *Neurophotonics* **5**, 1 (2018).
6. Denk, W., Strickler, J. H. & Webb, W. W. Two-Photon Laser Scanning Fluorescence Microscopy. *Science (1979)* **52**, 1778–1779 (1990).
7. Horton, N. G. *et al.* In vivo three-photon microscopy of subcortical structures within an intact mouse brain. *Nat Photonics* **7**, 205–209 (2013).
8. Rodríguez, C. *et al.* An adaptive optics module for deep tissue multiphoton imaging in vivo. *Nature Methods 2021 18:10* **18**, 1259–1264 (2021).
9. Zhang, Q. *et al.* Adaptive optics for optical microscopy [Invited]. *Biomedical Optics Express, Vol. 14, Issue 4, pp. 1732-1756* **14**, 1732–1756 (2023).
10. Ji, N. Adaptive optical fluorescence microscopy. *Nat Methods* **14**, 374–380 (2017).
11. Hampson, K. M. *et al.* Adaptive optics for high-resolution imaging. *Nature Reviews Methods Primers* vol. 1 1–26 Preprint at https://doi.org/10.1038/s43586-021-00066-7 (2021).
12. Babcock, H. W. THE POSSIBILITY OF COMPENSATING ASTRONOMICAL SEEING. *Publications of the Astronomical Society of the Pacific* **65**, 229 (1953).
13. Booth, M. J. Adaptive optical microscopy: The ongoing quest for a perfect image. *Light Sci Appl* **3**, 1–7 (2014).
14. Jacques, S. L. Optical properties of biological tissues: a review. *Phys Med Biol* **58**, R37 (2013).
15. Barad, Y., Eisenberg, H., Horowitz, M. & Silberberg, Y. Nonlinear scanning laser microscopy by third harmonic generation. *Appl Phys Lett* **70**, 922–924 (1997).
16. Squier, J. A., Müller, M., Brakenhoff, G. J. & Wilson, K. R. Third harmonic generation microscopy. *Opt Express* **3**, 315 (1998).

17. Cheng, J.-X. & Xie, X. S. Green's function formulation for third-harmonic generation microscopy. (2002) doi:10.1364/JOSAB.19.001604.

18. Weigelin, B., Bakker, G. J. & Friedl, P. Third harmonic generation microscopy of cells and tissue organization. *J Cell Sci* **129**, 245–255 (2016).

19. Chu, S. W., Tai, S. P., Ho, C. L., Lin, C. H. & Sun, C. K. High-resolution simultaneous three-photon fluorescence and third-harmonic-generation microscopy. *Microsc Res Tech* **66**, 193–197 (2005).

20. Fork, R. L., Greene, B. I. & Shank, C. V. Generation of optical pulses shorter than 0.1 psec by colliding pulse mode locking. *Appl Phys Lett* **38**, 671–672 (1981).

21. Xu, C., Nedergaard, M., Fowell, D. J., Friedl, P. & Ji, N. Multiphoton fluorescence microscopy for in vivo imaging. *Cell* **187**, 4458–4487 (2024).

22. Busch, W. *et al.* A microfluidic device and computational platform for high-throughput live imaging of gene expression. *Nat Methods* **9**, 1101–1106 (2012).

23. Jelínková, A. *et al.* Probing plant membranes with FM dyes: Tracking, dragging or blocking? *Plant Journal* **61**, 883–892 (2010).

24. Olivier, N., Débarre, D. & Beaurepaire, E. Dynamic aberration correction for multiharmonic microscopy. *Optics Letters, Vol. 34, Issue 20, pp. 3145-3147* **34**, 3145–3147 (2009).

25. Grieve, K. *et al.* Adaptive harmonic generation microscopy of mammalian embryos. *Optics Letters, Vol. 34, Issue 20, pp. 3154-3156* **34**, 3154–3156 (2009).

26. Thayil, A. & Booth, M. J. Self calibration of sensorless adaptive optical microscopes. *Journal of the European Optical Society-Rapid Publications* **6**, 11045 (2011).

27. Boyd, R. W. *Nonlinear Optics*. *Academic Press.* (Academic Press, Burlington, MA, 2020). doi:10.1016/C2015-0-05510-1.

28. Stock, C., Zlatanov, K. & Halfmann, T. Third harmonic generation and microscopy, enhanced by a bias harmonic field. *Opt Commun* **457**, 124660 (2020).

29. Schaller, R. D., Johnson, J. C. & Saykally, R. J. Nonlinear chemical imaging microscopy: Near-field third harmonic generation imaging of human red blood cells. *Anal Chem* **72**, 5361–5364 (2000).

30. Stock, C., Zlatanov, K. & Halfmann, T. Dispersion-enhanced third-harmonic microscopy. *Opt Commun* **393**, 289–293 (2017).

31. Jacobs, S. The optical heterodyne: key to advanced space signaling. *Electronics (Basel)* **29**, (1963).

32. Pawley, J. B. *Handbook of Biological Confocal Microscopy*. *Handbook of Biological Confocal Microscopy: Third Edition* (Springer, 2006). doi:10.1007/978-0-387-45524-2.

33. Marvin, M. Microscopy apparatus. *US Patent 3013467* (1957).

34. Hell, S., Reiner, G., Cremer, C. & Stelzer, E. H. K. Aberrations in confocal fluorescence microscopy induced by mismatches in refractive index. *J Microsc* **169**, 391–405 (1993).

35. Booth, M. J., Neil, M. A. A. & Wilson, T. Aberration correction for confocal imaging in refractive-index- mismatched media. *J Microsc* **192**, 90–98 (1998).

36. Schwertner, M., Booth, M. J., Neil, M. A. A. & Wilson, T. Measurement of specimen-induced aberrations of biological samples using phase stepping interferometry. *J Microsc* **213**, 11–19 (2004).

37. Booth, M. J. Adaptive optical microscopy: The ongoing quest for a perfect image. *Light Sci Appl* **3**, 1–7 (2014).

38. Ji, N. Adaptive optical fluorescence microscopy. *Nat Methods* **14**, 374–380 (2017).

39. Hampson, K. M. *et al.* Adaptive optics for high-resolution imaging. *Nature Reviews Methods Primers* vol. 1 1–26 Preprint at https://doi.org/10.1038/s43586-021-00066-7 (2021).

40. Zhang, Q. *et al.* Adaptive optics for optical microscopy [Invited]. *Biomedical Optics Express, Vol. 14, Issue 4, pp. 1732-1756* **14**, 1732–1756 (2023).

41. Tao, X. *et al.* Adaptive optics confocal microscopy using direct wavefront sensing. *Opt Lett* **36**, 1062 (2011).

42. Biss, D. P. *et al.* In vivo fluorescent imaging of the mouse retina using adaptive optics. *Opt Lett* **32**, 659 (2007).

43. Tao, X. *et al.* Adaptive optics microscopy with direct wavefront sensing using fluorescent protein guide stars. *Opt Lett* **36**, 3389 (2011).

44. Tao, X. *et al.* Live imaging using adaptive optics with fluorescent protein guide-stars. *Opt Express* **20**, 15969 (2012).

45. Shaw, M., O'Holleran, K. & Paterson, C. Investigation of the confocal wavefront sensor and its application to biological microscopy. *Opt Express* **21**, 19353 (2013).

46. Wang, K. *et al.* Rapid adaptive optical recovery of optimal resolution over large volumes. *Nat Methods* **11**, 625–628 (2014).

47. Wang, K. *et al.* Direct wavefront sensing for high-resolution in vivo imaging in scattering tissue. *Nat Commun* **6**, 1–6 (2015).

48. Booth, M. J., Neil, M. A. A., Juškaitis, R. & Wilson, T. Adaptive aberration correction in a confocal microscope. *Proc Natl Acad Sci U S A* **99**, 5788–5792 (2002).

49. Wahl, D. J., Huang, C., Bonora, S., Jian, Y. & Sarunic, M. V. Pupil segmentation adaptive optics for in vivo mouse retinal fluorescence imaging. *Opt Lett* **42**, 1365 (2017).

50. Ji, N., Milkie, D. E. & Betzig, E. Adaptive optics via pupil segmentation for high-resolution imaging in biological tissues. *Nat Methods* **7**, 141–147 (2010).

51. Ji, N., Sato, T. R. & Betzig, E. Characterization and adaptive optical correction of aberrations during in vivo imaging in the mouse cortex. *Proc Natl Acad Sci U S A* **109**, 22–27 (2012).

52. Milkie, D. E., Betzig, E. & Ji, N. Pupil-segmentation-based adaptive optical microscopy with full-pupil illumination. **36**, 4206–4208 (2011).

53. Wang, C. *et al.* Multiplexed aberration measurement for deep tissue imaging in vivo. *Nat Methods* **11**, 1037–1040 (2014).

54. Liu, R., Milkie, D. E., Kerlin, A., MacLennan, B. & Ji, N. Direct phase measurement in zonal wavefront reconstruction using multidither coherent optical adaptive technique. *Opt Express* **22**, 1619 (2014).

55. Pan, D. *et al.* Frequency-multiplexed aberration measurement for confocal microscopy. *Optics Express, Vol. 32, Issue 16, pp. 28655-28665* **32**, 28655–28665 (2024).

56. Matlashov, M. E. *et al.* A set of monomeric near-infrared fluorescent proteins for multicolor imaging across scales. *Nat Commun* **11**, 1–12 (2020).

57. Wang, C. *et al.* Multiplexed aberration measurement for deep tissue imaging in vivo. *Nat Methods* **11**, 1037–1040 (2014).

58. Einstein, A. Über einen die Erzeugung und Verwandlung des Lichtes betreffenden heuristischen Gesichtspunkt. *Ann Phys* **322**, 132–148 (1905).

59. Göppert-Mayer, M. Über Elementarakte mit zwei Quantensprüngen. *Ann Phys* **401**, 273–294 (1931).

60. Drobizhev, M., Makarov, N. S., Tillo, S. E., Hughes, T. E. & Rebane, A. Two-photon absorption properties of fluorescent proteins. *Nature Methods 2011 8:5* **8**, 393–399 (2011).

61. Sinefeld, D. *et al.* Comparing the effective attenuation lengths for long wavelength in vivo imaging of the mouse brain. *Biomedical Optics Express, Vol. 9, Issue 8, pp. 3534-3543* **9**, 3534–3543 (2018).

62. Campagnola, P. J. *et al.* Three-Dimensional High-Resolution Second-Harmonic Generation Imaging of Endogenous Structural Proteins in Biological Tissues. *Biophys J* **82**, 493–508 (2002).

63. Correa-García, S., Pande, P., Séguin, A., St-Arnaud, M. & Yergeau, E. Rhizoremediation of petroleum hydrocarbons: a model system for plant microbiome manipulation. *Microb Biotechnol* **11**, 819–832 (2018).

64. Calleja-Cabrera, J., Boter, M., Oñate-Sánchez, L. & Pernas, M. Root Growth Adaptation to Climate Change in Crops. *Frontiers in Plant Science* vol. 11 Preprint at https://doi.org/10.3389/fpls.2020.00544 (2020).

65. Lux, A. & Rost, T. L. Plant root research: the past, the present and the future. *Ann Bot* **110**, 201–204 (2012).

66. Bishopp, A. & Lynch, J. P. The hidden half of crop yields. *Nat Plants* **1**, 1–2 (2015).

67. Ledford, H. The lost art of looking at plants. *Nature* **553**, 396–398 (2018).

68. Eshel, A. & Beeckman, T. *Plant Roots: The Hidden Half*. (CRC Press, Boca Raton, 2013).

69. Zengler, K. *et al.* EcoFABs: advancing microbiome science through standardized fabricated ecosystems. *Nat Methods* **16**, 567–571 (2019).

70. Sasse, J. *et al.* Multilab EcoFAB study shows highly reproducible physiology and depletion of soil metabolites by a model grass. *New Phytologist* (2019) doi:10.1111/nph.15662.

71. Jabusch, L. K. *et al.* Microfabrication of a chamber for high-resolution, in situ imaging of the whole root for plant–microbe interactions. *Int J Mol Sci* **22**, (2021).

72. Truernit, E. *et al.* High-resolution whole-mount imaging of three-dimensional tissue organization and gene expression enables the study of phloem development and structure in Arabidopsis. *Plant Cell* **20**, 1494–1503 (2008).

73. Maizel, A., Von Wangenheim, D., Federici, F., Haseloff, J. & Stelzer, E. H. K. High-resolution live imaging of plant growth in near physiological bright conditions using light sheet fluorescence microscopy. *Plant Journal* **68**, 377–385 (2011).

74. de Luis Balaguer, M. A. *et al.* Multi-sample Arabidopsis Growth and Imaging Chamber (MAGIC) for long term imaging in the ZEISS Lightsheet Z.1. *Dev Biol* **419**, 19–25 (2016).

75. von Wangenheim, D. *et al.* Early developmental plasticity of lateral roots in response to asymmetric water availability. *Nat Plants* **6**, 73–77 (2020).

76. Grossmann, G. *et al.* Green light for quantitative live-cell imaging in plants. *J Cell Sci* **131**, (2018).

77. Clark, N. M. *et al.* Novel Imaging Modalities Shedding Light on Plant Biology: Start Small and Grow Big. *Annu Rev Plant Biol* **71**, 789–816 (2020).

78. Hériché, M., Arnould, C., Wipf, D. & Courty, P. E. Imaging plant tissues: advances and promising clearing practices. *Trends Plant Sci* **27**, 601–615 (2022).

79. Feijó, J. A. & Moreno, N. Imaging plant cells by two-photon excitation. *Protoplasma* **223**, 1–32 (2004).

80. Mizuta, Y., Kurihara, D. & Higashiyama, T. Two-photon imaging with longer wavelength excitation in intact Arabidopsis tissues. *Protoplasma* **252**, 1231–1240 (2015).

81. Bureau, C. *et al.* A protocol combining multiphoton microscopy and propidium iodide for deep 3D root meristem imaging in rice: Application for the screening and identification of tissue-specific enhancer trap lines. *Plant Methods* **14**, 1–9 (2018).

82. Lee, J. *et al.* Label-Free Multiphoton Imaging of Microbes in Root, Mineral, and Soil Matrices with Time-Gated Coherent Raman and Fluorescence Lifetime Imaging. *Environ Sci Technol* **56**, 1994–2008 (2022).

83. Chochois, V., Vogel, J. P. & Watt, M. Application of Brachypodium to the genetic improvement of wheat roots. *J Exp Bot* **63**, 3467–3474 (2012).

84. Brutnell, T. P. Model grasses hold key to crop improvement. *Nature Plants* vol. 1 1–3 Preprint at https://doi.org/10.1038/NPLANTS.2015.62 (2015).

85. Provart, N. J. *et al.* 50 years of Arabidopsis research: Highlights and future directions. *New Phytologist* **209**, 921–944 (2016).

86. Milkie, D. E., Betzig, E. & Ji, N. Pupil-segmentation-based adaptive optical microscopy with full-pupil illumination. *Opt Lett* **36**, 4206–4208 (2011).

87. Akturk, S., Xun, G. & Trebino, R. Extremely simple ultrashort-pulse compressor. *Conference on Lasers and Electro-Optics and 2006 Quantum Electronics and Laser Science Conference, CLEO/QELS 2006* **14**, 10101–10108 (2006).

88. Vogel, J. P., Garvin, D. F., Leong, O. M. & Hayden, D. M. Agrobacterium-mediated transformation and inbred line development in the model grass Brachypodium distachyon. *Plant Cell Tissue Organ Cult* **84**, 199–211 (2006).

89. González-Pérez, E. *et al.* The Arabidopsis-Trichoderma interaction reveals that the fungal growth medium is an important factor in plant growth induction. *Sci Rep* **8**, 1–14 (2018).

90. Lin, H.-H. *et al.* Impact of inoculation practices on microbiota assembly and community stability in a fabricated ecosystem. *Phytobiomes J* **3**, 1–66 (2015).

91. Wang, B. *et al.* CRAGE-Duet Facilitates Modular Assembly of Biological Systems for Studying Plant-Microbe Interactions. *ACS Synth Biol* **9**, 2610–2615 (2020).

92. Schindelin, J. *et al.* Fiji: An open-source platform for biological-image analysis. *Nat Methods* **9**, 676–682 (2012).

93. Akturk, S., Xun, G. & Trebino, R. Extremely simple ultrashort-pulse compressor. *Conference on Lasers and Electro-Optics and 2006 Quantum Electronics and Laser Science Conference, CLEO/QELS 2006* **14**, 10101–10108 (2006).

94. Gao, J. *et al.* Ecosystem Fabrication (EcoFAB) Protocols for The Construction of Laboratory Ecosystems Designed to Study Plant-microbe Interactions. *J Vis Exp* **2018**, (2018).

95. Débarre, D. *et al.* Imaging lipid bodies in cells and tissues using third-harmonic generation microscopy. *Nat Methods* **3**, 47–53 (2006).

96. Gausman, H. W., Allen, W. A. & Escobar, D. E. Refractive Index of Plant Cell Walls. *Appl Opt* **13**, 109 (1974).

97. Liu, P. Y. *et al.* Cell refractive index for cell biology and disease diagnosis: Past, present and future. *Lab on a Chip* vol. 16 634–644 Preprint at https://doi.org/10.1039/c5lc01445j (2016).

98. Crang, R., Lyons-Sobaski, S. & Wise, R. *Plant Anatomy*. (Springer International Publishing, 2018). doi:10.1007/978-3-319-77315-5.

99. Hawes, M. C. & Lin, H. J. Correlation of pectolytic enzyme activity with the programmed release of cells from root caps of pea (Pisum sativum). *Plant Physiol* **94**, 1855–1859 (1990).

100. Mravec, J. Border cell release: Cell separation without cell wall degradation? *Plant Signal Behav* **12**, 1–3 (2017).

101. Pan, D. *et al.* Label-free structural imaging of plant roots and microbes using third-harmonic generation microscopy. *bioRxiv* 2024.04.13.589377 (2024) doi:10.1101/2024.04.13.589377.

102. Gupta, D. S. & Ibaraki, Y. *Plant Image Analysis: Fundamentals and Applications*. (2014).

103. Munakata, R. *et al. Recent Advances in Polyphenol Research*. *Polyphenols from Plant Roots* vol. 8 (John Wiley & Sons, Ltd, Chichester, UK, 2019).

104. Donaldson, L. Autofluorescence in plants. *Molecules* **25**, (2020).

105. Naseer, S. *et al.* Casparian strip diffusion barrier in Arabidopsis is made of a lignin polymer without suberin. *Proc Natl Acad Sci U S A* **109**, 10101–10106 (2012).

106. Dong, B. *et al.* Superresolution intrinsic fluorescence imaging of chromatin utilizing native, unmodified nucleic acids for contrast. *Proc Natl Acad Sci U S A* **113**, 9716–9721 (2016).

107. Kalinina, N. O., Makarova, S., Makhotenko, A., Love, A. J. & Taliansky, M. The multiple functions of the nucleolus in plant development, disease and stress responses. *Front Plant Sci* **9**, 1–19 (2018).

108. Kim, K. & Guck, J. The Relative Densities of Cytoplasm and Nuclear Compartments Are Robust against Strong Perturbation. *Biophys J* **119**, 1946–1957 (2020).

109. Dvořáčková, M. & Fajkus, J. Visualization of the nucleolus using ethynyl uridine. *Front Plant Sci* **9**, 1–8 (2018).

110. Wang, Z. *et al.* Dehydration of plant cells shoves nuclei rotation allowing for 3D phase-contrast tomography. *Light Sci Appl* **10**, (2021).

111. Verma, D. P. S. Cytokinesis and building of the cell plate in plants. *Annu Rev Plant Physiol Plant Mol Biol* **52**, 751–784 (2001).

112. Beneš, K. & Kutík, J. The localization of starch in root tips. *Biol Plant* **20**, 458–463 (1978).

113. Jang, G. J., Jang, J. C. & Wu, S. H. Dynamics and functions of stress granules and processing bodies in plants. *Plants* vol. 9 1–11 Preprint at https://doi.org/10.3390/plants9091122 (2020).

114. Lugtenberg, B. *Principles of Plant-Microbe Interactions: Microbes for Sustainable Agriculture*. *Principles of Plant-Microbe Interactions: Microbes for Sustainable Agriculture* (2015). doi:10.1007/978-3-319-08575-3.

115. Czymmek, K. J., Duncan, K. E. & Berg, H. Realizing the Full Potential of Advanced Microscopy Approaches for Interrogating Plant-Microbe Interactions. *Molecular Plant-Microbe Interactions* **36**, 245–255 (2023).

116. Bissett, J. Trichoderma atroviride. *Canadian Journal of Botany* **70**, 639–641 (1992).

117. Druzhinina, I. S. *et al.* Trichoderma: The genomics of opportunistic success. *Nat Rev Microbiol* **9**, 749–759 (2011).

118. Navazio, L. *et al.* Calcium-mediated perception and defense responses activated in plant cells by metabolite mixtures secreted by the biocontrol fungus Trichoderma atroviride. *BMC Plant Biol* **7**, 1–9 (2007).

119. Brutnell, T. P., Bennetzen, J. L. & Vogel, J. P. Brachypodium distachyon and Setaria viridis: Model Genetic Systems for the Grasses. *Annu Rev Plant Biol* **66**, 465–485 (2015).

120. Vogel, J. P. *Genetics and Genomics of Brachypodium*. *Plant Genetics and Genomics: Crops and Models* vol. 18 (Springer International Publishing, Cham, 2016).

121. Cheng, P. chin *et al.* Multi-photon fluorescence microscopy - The response of plant cells to high intensity illumination. *Micron* **32**, 661–669 (2001).

122. Cox, G., Moreno, N. & Feijó, J. Second-harmonic imaging of plant polysaccharides. *J Biomed Opt* **10**, 024013 (2005).

123. Hallmann, J., Quadt-Hallmann, A., Miller, W. G., Sikora, R. A. & Lindow, S. E. Endophytic colonization of plants by the biocontrol agent Rhizobium etli G12 in relation to Meloidogyne incognita infection. *Phytopathology* **91**, 415–422 (2001).

124. Byrt, C. S., Munns, R., Burton, R. A., Gilliham, M. & Wege, S. Root cell wall solutions for crop plants in saline soils. *Plant Science* **269**, 47–55 (2018).

125. Planchon, T. A. *et al.* Adaptive correction of a tightly focused, high-intensity laser beam by use of a third-harmonic signal generated at an interface. *Opt Lett* **31**, 2214 (2006).

126. Ji, N., Liang, Y. & Turcotte, R. Adaptive optical versus spherical aberration corrections for in vivo brain imaging. *Biomedical Optics Express, Vol. 8, Issue 8, pp. 3891-3902* **8**, 3891–3902 (2017).

127. Shen, Y. R. *The Principles of Nonlinear Optics*. (Wiley, 2003).

128. Chang, C. F., Yu, C. H. & Sun, C. K. Multi-photon resonance enhancement of third harmonic generation in human oxyhemoglobin and deoxyhemoglobin. *J Biophotonics* **3**, 678–685 (2010).

129. Siegman, A. E., Harris, S. E. & McMurtry, B. J. Optical heterodyning and optical demodulation at microwave frequencies. *Optical Masers* **13**, 511–528 (1963).

130. Thiansathaporn, P. & Superfine, R. *Homodyne Surface Second-Harmonic Generation*. *OPTICS LETTERS* vol. 20 (1995).

131. Chen, J., Machida, S. & Yamanoto, Y. Simultaneous measurement of amplitude and phase in surface second-harmonic generation. *Opt Lett* **23**, 676 (1998).

132. Yazdanfar, S., Laiho, L. H. & So, P. T. C. Interferometric second harmonic generation microscopy. *Opt Express* **12**, 2739 (2004).

133. Goodman, A. J. & Tisdale, W. A. Enhancement of second-order nonlinear-optical signals by optical stimulation. *Phys Rev Lett* **114**, (2015).

134. Marx, C. A., Harbola, U. & Mukamel, S. Nonlinear optical spectroscopy of single, few, and many molecules: Nonequilibrium Greena's function QED approach. *Phys Rev A* **77**, (2008).

135. Goodman, A. J. & Tisdale, W. A. Goodman and Tisdale Reply. *Phys Rev Lett* **116**, 059402 (2016).

136. Chang, R. K., Ducuing, J. & Bloembergen, N. Relative phase measurement between fundamental and second-harmonic light. *Phys Rev Lett* **15**, 6–8 (1965).

137. Veenstra, K. J., Petukhov, A. V, De Boer, A. P. & Rasing, T. Phase-sensitive detection technique for surface nonlinear optics. *Phys Rev B* **58**, 16020–16023 (1998).

138. Rechsteiner, P., Hulliger, J. & Flörsheimer, M. Phase-sensitive second harmonic microscopy reveals bipolar twinning of Markov-type molecular crystals. *Chemistry of Materials* **12**, 3296–3300 (2000).

139. Rivard, M. *et al.* Imaging the bipolarity of myosin filaments with Interferometric Second Harmonic Generation microscopy. *Biomed Opt Express* **4**, 2078 (2013).

140. Rivard, M. *et al.* Imaging the noncentrosymmetric structural organization of tendon with Interferometric Second Harmonic Generation microscopy. *J Biophotonics* **7**, 638–646 (2014).

141. Bancelin, S. *et al.* Probing microtubules polarity in mitotic spindles in situ using Interferometric Second Harmonic Generation Microscopy. *Sci Rep* **7**, 1–8 (2017).

142. Gao, Y., Goodman, A. J., Shen, P. C., Kong, J. & Tisdale, W. A. Phase-Modulated Degenerate Parametric Amplification Microscopy. *Nano Lett* **18**, 5001–5006 (2018).